Chapter 3

Studies on 1, 3-disulfoimidazolium chloronickellate immobilized HZSM-5 framework as visible-light induced heterogeneous photocatalyst for degradation of organic dye using advanced oxidation process

Published with modification

Saikia, S., Gogoi, P. and Borah, R. 1, 3-Disulfoimidazolium chloronickellate immobilized HZSM-5 framework as visible-light-induced heterogeneous photocatalyst for advanced oxidation process. *New Journal of Chemistry*, 42(5):3867-3877, 2018.

3A.1 Zeolites

In depth description of zeolites covers a wide space which already has been explored by many scientists. Zeolites are microporous crystalline aluminosilicates comprising of three dimensional framework of interconnected TO_4 tetrahedra (T = Si^{4+}, Al^{3+}) containing oxygen atoms [1-4]. The replacement of Si^{4+} cations of uncharged silica framework (SiO_2) with Al^{3+} cations makes the framework negatively charged and thus it requires the presence of extraframework singly or doubly-charged cations, such as alkali or alkaline earth metals to keep the overall framework neutral [4-6]. The composition of zeolite can be expressed as a combination of three components:

$M^{m+}_{n/m}$	•	$Si_{1-n}Al_nO_2$	•	nH_2O
Extraframework cations		**Framework**		**Sorbed phase**

The extraframework cations mainly take part in ion-exchange chemistry of these materials. The arrangement of $[SiO_4]^{4-}$ and $[AlO_4]^{5-}$ tetrahedra within the framework of zeolite develops voids or pores between the tetrahedra in the form of cages or channels (**Fig.3A.1**).

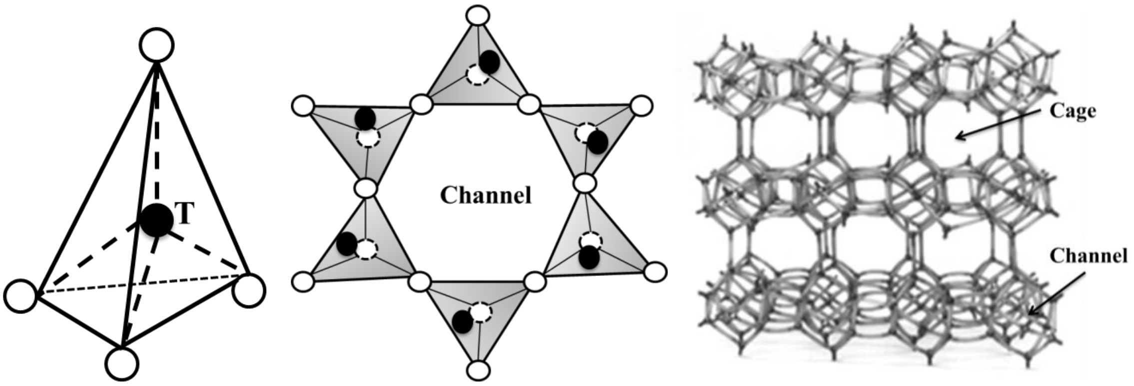

(a) (b) (c)

Fig.3A.1: (a) Tetrahedral structure of TO_4 unit (T = Si, Al), (b) Single ring tetrahedron structure of zeolite framework & (c) Typical zeolite structure showing three dimensional cages and channels

The structural formula of zeolite can be written as $M_{a/n}(AlO_2)_a.(SiO_2)_b.wH_2O$ derived from its crystal unit cell compositions where **a** and **b** are total numbers of tetrahedra of Al and Si respectively per unit cell; **w** is the number of water molecules per unit cell. The Si/Al ratio (b/a values) values indicate the amount of Al within the framework which can vary over wide range from 1 to infinity (∞), expressing only siliceous form of the framework. The lower limit of Si/Al = 1 can be accounted for displacing of two AlO_4^- tetrahedra because of electrostatic repulsions between the negative charges as proposed by Löwenstein [7]. The variation of Si/Al ratio leads to structural and behavioral changes among various types of zeolites. For example, hydrothermal stability and hydrophobicity of the framework increases as the ratio of Si/Al increases. The Si/Al ratio usually varies from 1 to 5. Most natural zeolites are known with lower Si/Al ratios. The discovery of low silica **A** and **X** zeolites (Si/Al<1.5) by Milton and Breck at Union Carbide in 1959 was followed by the synthesis of Y zeolite in 1964 with an intermediate range of Si/Al ratios of 1.5-3.8. The low silica zeolites suffer a chemical change known as “dealumination’’ in presence of acids or steam treatment at elevated temperature, thus restrict their use in acid catalyzed organic reactions [8].

Ruscher *et al.* [8] observed dealumination of the Y zeolite with Si/Al ratio 2.2 using the steam treatment method without collapsing its framework. Highly siliceous zeolite structure like ZSM-5 with Si/Al ratios in between 10-100 are known to be stable towards dealuminating condition at elevated temperature [5, 9, 10], whereas pure silica zeolites are stable in all mineral acids except HF acid. The thermal property study reveals extreme high thermal stability of siliceous zeolites up to 1000^oC.

The presence of open channels and pores initiates easy accommodation of some specific cations, water molecules and some organic molecules into the zeolite framework. Also loosely bound ions or molecules of the zeolite cages can be removed or exchanged without disturbing the original structure. The ion exchange and adsorption capacity of zeolites are correlated with its surface area and pore sizes. The surface also introduces various physical interactions for the control of hydrophobicity, hydrophilicity and binding to reactant molecules. These surface properties have been gaining attention due to their role in framework modification through which zeolite structure can be modified on the basis of certain applications they tend to perform. Thus, zeolite has become a significant tool to improvise different areas of chemistry [11].

3A.2 ZSM-5: An insight into framework behavior

Structure of ZSM-5

The structure of ZSM-5 belongs to pentasil family of zeolites having chemical formula $Na_nAl_nSi_{96}–nO_{192}·16H_2O$ (0<n<27) (**Fig.3A.2**). Structural composition of ZSM-5 bears several pentasil units linked together by oxygen bridges to form pentasil chains and each pentasil unit consists of eight five-membered rings in which the vertices are Al and Si. An O atom is considered to be bonded between the vertices. Oxygen bridges interconnect the pentasil chains forming channeled sheets with 10-ring holes and each hole has similar arrangement of Al, Si and O like pentasil unit. The sheets formed by oxygen bridges linked to pentasil chain possess straight 10-ring channels running parallel to the corrugations and sinusoidal 10-ring channels perpendicular to the sheets [12]. ZSM-5 has pore diameter range of 5 Å and it has Si/Al ratio more than five. ZSM-5 is a medium pore zeolite having pore size (0.54 nm × 0.56 nm) and has two intersecting three-dimensional channels with one straight parallel channel and the other running parallel defined by sinusoidal 10-membered ring openings of 5.3 Å × 5.6 Å and 5.1 Å × 5.5 Å [13]. ZSM-5 has 96 T sites (Si or Al), 192 O sites, and a number of compensating cations in the crystallographic unit cell depending on the Si/Al ratio, which ranges from 12 to infinity. The structure appears to be orthorhombic at high temperatures which undergoes a phase transition to the monoclinic on cooling below the transition temperature, located between 300 and 350 K [14, 15].

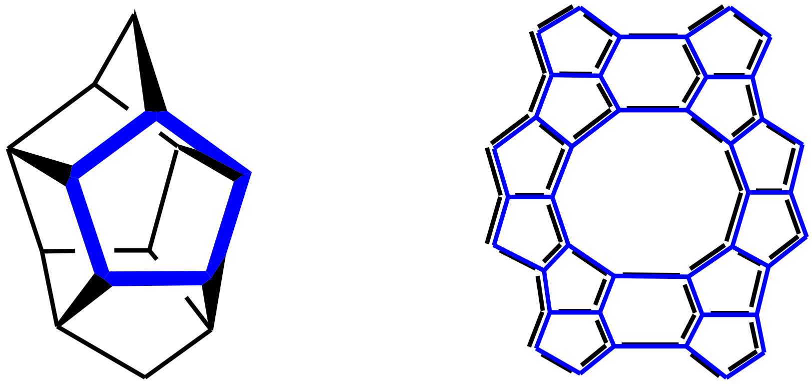
(a) (b)

Fig.3A.2: (a) Pentasil unit of ZSM-5 and (b) Structure of ZSM-5

Modification of ZSM-5 structure via dealumination, realumination and desilication techniques

As mentioned in earlier section, dealumination is an effective chemical modification step for controlling the acidity of zeolitic materials *via* removal of framework Al (FAl) atoms using various methods like steaming, calcinations, acid treatment, ammonium hexafluorosilicate treatment *etc.* without disturbing micropore structures of the zeolites [16-19]. Extra framework Al (EFAls) species such as $Al(OH)^+$, AlO^+ *etc.* are formed during this process and they act as true carrier of Lewis acidity of the modified structure. ZSM-5 zeolite is more resistant to this treatment unlike zeolite-Y because of its unique shape selective MFI structure, lower Al content and greater thermal stability. The most widely used dealumination techniques are steaming and acid treatments [20]. The effects of dealumination on HZSM-5 caused by steaming produce significant change of -OH stretching frequencies of Brönsted acidic bridging hydroxyl groups (Si(OH)Al) at 3610 cm^{-1} related to the FAl species [21] and at 3667 cm^{-1} for the -OH group directly attached to the EFAl species [22, 23]. The band associated with the -OH stretching mode of terminal silanol group (SiOH) was observed at 3743 cm^{-1} [24]. The presence of such terminal and internal silanol (SiOH) groups in ZSM-5 was studied by Chester *et a1.* and this was later established by NMR spectroscopy that the internal SiOH groups formed defective sites in zeolite crystals [25, 26]. The behavior of these silanol groups have been widely investigated by many researchers through IR spectroscopy [27-30].

Kraushaar *et al.* [31, 32] analyzed the nature of internal SiOH groups by silylation with trimethylsilyl chloride and ^{29}Si MAS NMR analysis indicated that these silanol groups existed as a nest of four SiOH groups typically called ‘hydroxyl nest’, where, the T atom is missing from the ZSM-5 framework. In spite of the insufficient data to support the concept of hydroxyl nest as reported by Dessau *et al.* [33], it was highly involved in dehydroxylation dealumination mechanism of ZSM-5. The following equation (**Scheme 3A.1**) depicts the generation of the “hydroxyl nest” on acid dealumination which was further considered for destruction of the zeolite structure [34]:

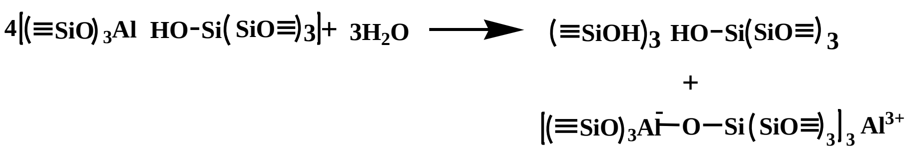

$$4[(\equiv SiO)_3Al\ \ HO{-}Si(SiO\equiv)_3] + 3H_2O \longrightarrow (\equiv SiOH)_3\ HO{-}Si(SiO\equiv)_3 + [(\equiv SiO)_3\bar{Al}{-}O{-}Si(SiO\equiv)_3]_3\,Al^{3+}$$

Scheme 3A.1: Formation of “hydroxyl nest”

Hydrothermal dealumination of HZSM-5 often proceeds with partial destruction of parent structure with formation of defective sites resulting in loss of crystallinity [35, 36]. Infrared region in between 1300-400 cm^{-1} was used to observe the structural change of aluminosilicate lattice relating to T-O-T asymmetric and symmetric stretching vibrations at 800 and 1087 cm^{-1} [37]. The absorption bands at 544 and 1219 cm^{-1} were assigned for vibrations associated with structural assembly of interconnected TO_4 in HZSM-5. Any modification of the parent HZSM-5 structure causes a small shift of wave number for one of the structure sensitive double ring vibration at 544 cm^{-1} [35, 38], in contrast to insensitive vibration at 800 cm^{-1} for the T-O-T asymmetric stretching belong to the TO_4 tetrahedra. The ratios between the absorbance of these bands are analyzed as the extent of crystallinity that ZSM-5 framework bears after dealumination.

Reinsertion of the EFAl species in to the parent HZSM-5 structure after steaming of the HZSM-5 was investigated by different groups using acid leaching to prevent the detrimental effects of EFAls in catalysis and transport properties [38, 39]. But the leaching method was not successful with mineral acids (such as HCl), leading to further dealumination after steaming [40]. Other reports explained that reinsertion of the framework Al occurred through the treatment of the dealuminated ZSM-5 obtained from hydrothermal method with basic solutions or $AlCl_3$ vapour which maintained the acidity and activity of high silica zeolites [41-44]. Omegna *et al.* reexamined the effect of mineral acid treatment in reinsertion of non-framework Al atoms into the lattice of dealuminated HZSM-5 and observed that instead of realumination, further dealumination occurred [45]. This analysis opposed the claim of reinsertion of the non-framework Al into the dealuminated HZSM-5 after treatment with mineral acid as reported by San *et al.* [46]. Fan *et al.* [47] elaborated the influence of citric acid on HZSM-5 after steaming and its effect on Al state, acidity and porosity accordingly. He examined two kinds of acid treatments on the dealuminated HZSM-5 in presence of HCl/citric acids, demonstrating distinct structural changes of the EFAl species for the citric acid treatment. The citric acid treatment showed higher intensity of the peak at 3610 cm^{-1} for the FAl species in contrast to reduction of peak intensity of the O-H band at 3667 cm^{-1} for the dealuminated Al atoms. The unusual increased amount of the FAl after steaming was accounted for reinsertion of the EFAls into the defective sites of steamed HZSM-5 framework. The realumination of the HZSM-5 zeolite was also confirmed using ^{27}Al MAS NMR spectroscopy.

Despite of the advantageous feature of shape selectivity of the ZSM-5 zeolites, the relatively small pore size intrinsically induces a restricted physical transport of molecules to and from the active acid sites located in the micropores. Thus, they often have negative impact on the catalytic activity. Therefore, modification of the siliceous ZSM-5 zeolites can also be achieved upon dissolution of amorphous silica in alkaline medium for generation of mesoporous structure with preserved structural integrity which may increase the transport ability of bulky reactant or product molecules in large space mesopore materials around an active catalytic site [48]. This desilication process is very effective for the preparation of active mesoporous ZSM-5 materials with improved catalytic activity in gasoline production, hexane cracking, cyclohexene conversion, Fischer-Tropsch synthesis *etc.* [49-51].

3A.3 ZSM-5 as better support

Selection of zeolite support for immobilization of catalytically active metals, metal oxides, metal salts, metal complexes, acidic compounds, nano materials *etc.* is considered from its unique shape selectivity, solid acidity, ion exchangeability, pore size, thermal stability and structural network [52-60]. The presence of medium pore size (5.1-5.6 Å) bearing three dimensional channels defined by 10-membered rings and smaller crystallite sizes of ZSM-5 framework can work as better support for immobilization of active catalytic species on its surface [61, 62]. Furthermore, high content of Si/Al ratio of the ZSM-5 support prevents dealumination of framework Al which is a common problem of many other zeolites to use as support for immobilization of acidic material.

A large number of zeolite supported catalytic systems have been developed for efficient utilization as heterogeneous catalysts in organic synthesis [63, 64]. Metal catalysts can be readily dispersed due to the surface properties and negatively charged framework of the zeolite which favor enhancement of metal-support interaction [65, 66]. Also, interaction of organic substrates with acidic or basic sites of zeolite and modification of electronic properties of the metal species by zeolite framework lead supported catalysts towards high activity and selectivity [65-69]. Furthermore, the porosity possessed by zeolite may control significant transfer of selective masses of reactants and products, thus enhancing the selectivity of reaction. This established that the hierarchically porous zeolites could be a better candidate for designing new functional metal catalysts with high activity and good selectivity (**Fig. 3A.3**) [70]. Nonetheless, modification of acidity, pore structure by dealumination or desilication causes significant contribution to prepare a ZSM-5 support with greater quality while the high silica ZSM-5 is already quite fruitful as a support material.

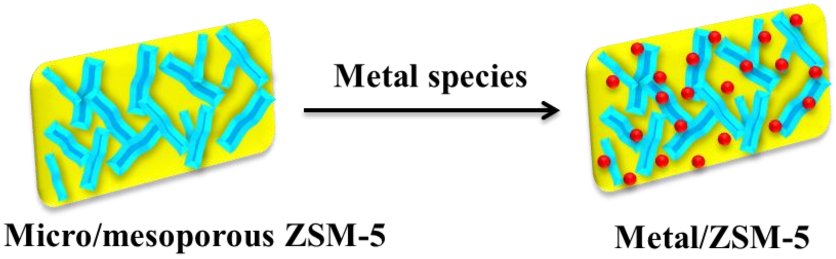

Fig.3A.3: Metal immobilized ZSM-5

3A.4 Ionic liquid immobilized ZSM-5

Various factors responsible for better performance of ZSM-5 as support material during immobilization of metal species, metal complexes, metal salts, nanomaterials, ionic liquids or salts are already discussed in the previous **Section 3A.3.** A number of composite materials derived from ionic liquid supported zeolites have been developed for catalysis or applications in other areas of chemistry involve Y-zeolites, mordenites, BETA, ZSM-5 *etc.* [71-73]. It is obvious that heterogenization transfers acidic, basic or other physical character of the ionic liquids to the support at the cost of elimination of bulk properties such as viscosity, conductivity, density, liquid state *etc.* Similarly the support also provides high surface area, Brönsted acidity and greater thermal stability to the composite material. This section includes the literature review of the limited works on ZSM-5 supported ionic liquid systems designed till 2017.

Jin and his coworkers in 2009 immobilized palladium acetate in thin ionic liquid layers on the mesopore wall of hierarchical MFI zeolite according to **Scheme 3A.2** and efficiently examined as recyclable heterogeneous catalyst for Suzuki coupling reaction of various aryl bromides with arylboronic acids in water (**Scheme 3A.3**) [64]. The two step catalyst preparation involved anchoring of 1-(3-triethoxysilylpropyl)-3-methylimidazolium chloride ([tpim][Cl]) on the mesopore walls of MFI zeolite followed by immobilization of palladium acetate in 1-butyl-3-methylimidazolium hexafluorophosphate ([bmim][PF_6]).

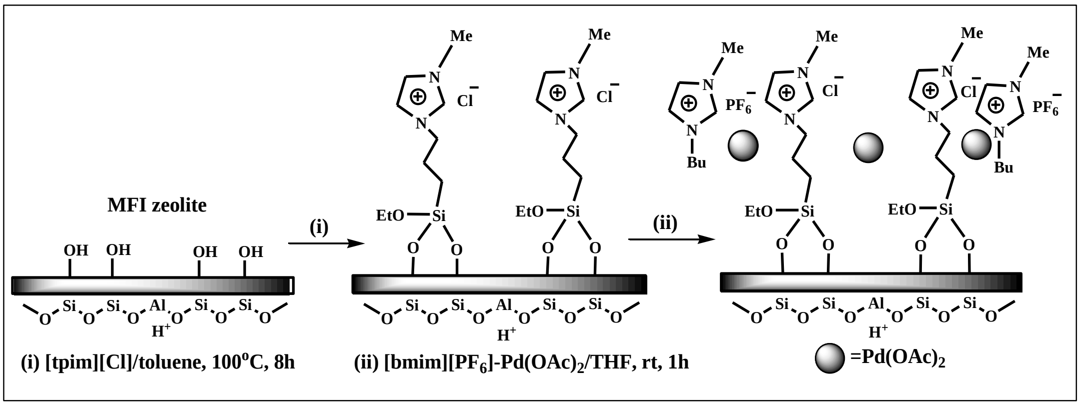

Scheme 3A.2: Synthesis of [bmim][PF_6]- $Pd(OAc)_2$ immobilized ionic liquid functionalized MFI catalyst

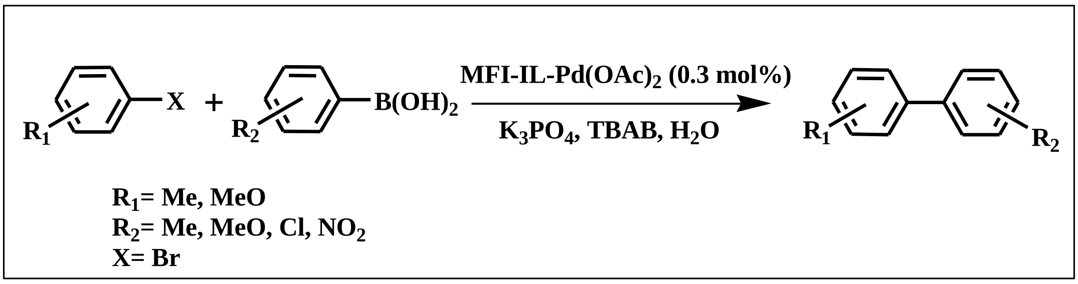

Scheme 3A.3: Suzuki coupling reaction catalyzed by IL supported catalyst

Arya *et al.* (2012) prepared two ZSM-5 supported acidic ionic liquid catalysts consisting of Brönsted acidic ionic liquids (BAILs) 1-methylimidazolium tetrafluoroborate ([mim][BF_4]) and 1-butyl-3-methylimidazolium tetrafluoroborate ([bmim][BF_4]) in water. They employed these ZSM-5 supported ionic liquids ZSM-5-([mim][BF_4]) and ZSM-5-([bmim][BF_4]) in the synthesis of a library of novel N-substituted spiro[indolepyridothiazine] analogs in water (**Scheme 3A.4**). Variation of molar ratio of substrate with ZSM-5 supported ionic liquids gave an optimum molar ratio 1:1 to produce satisfactory yield of the product. Also among the two ionic liquids used, the shorter chain cation ([mim][BF_4]) seemed to be better than the longer chain cation containing ionic liquid ([bmim][BF_4]) [74].

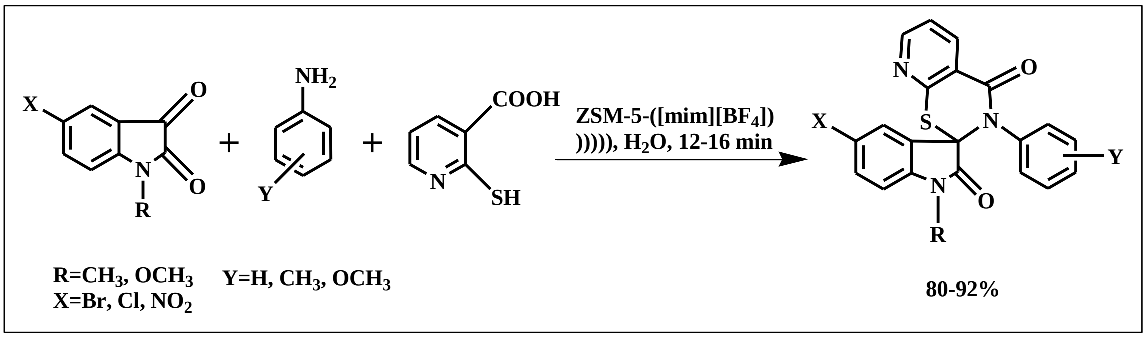

Scheme 3A.4: ZSM-5-([mim][BF$_4$]) catalyzed synthesis of spiro[N-substituted indole-pyridothiazines]

In 2013, the same group again synthesized BAIL confined ZSM-5 catalytic system ZSM-5-([bmim][BF$_4$]) using 1-butyl-3-methylimidazolium tetrafluoroborate ionic liquid and tested their catalytic activity in aqueous media at room temperature for the greener synthesis of spiro[pyrazolo[3, 4-e]benzothiazepine] analogues in higher yield with shorter reaction time for the first time (**Scheme 3A.5**) [75]. The catalytic system was found to be recyclable up to five times without significant loss of yield.

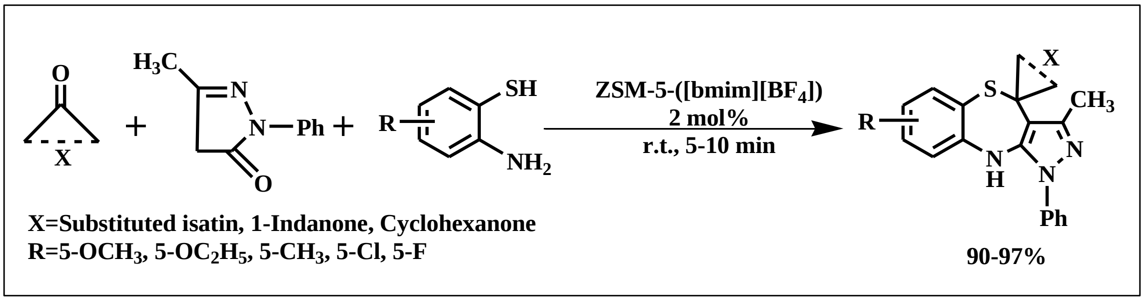

Scheme 3A.5: Synthesis of spiro [pyrazolo[3, 4-e][1,5]benzothiazepine] derivatives

Murthy *et al.* (2013) [76] designed 1-butyl-3-methylimidazolium tetrafluoroborate impregnated Sn-ZSM-5 membrane to separate butyl acetate-water mixtures by pervaporation. Higher affinity of ionic liquid for butyl acetate increases the permeability of membrane more than 1.5 times. They observed that the maximum separation factor α of more than 326 was found for a 0.6 weight % aqueous butyl acetate solution at 323 K for IL-Sn-ZSM-5 membrane.

Shindo and his coworkers (2014) [77] developed composite membranes of polyimide (PI), 1-butyl-3-methyl-imidazolium bis(trifluoromethyl-sulfonyl)imide ([C$_4$mim][Tf$_2$N]) ionic liquid (**Fig.3A.4**) and ZSM-5 by solvent casting method to study the effects of zeolites on gas permeation properties. Thermal stability of the composite membranes improved upon addition of the IL and ZSM-5 into the polyimide. The CO_2 permeable selectivity of PI+IL+ZSM-5 membranes was higher than that of the PI + ZSM-5 membrane.

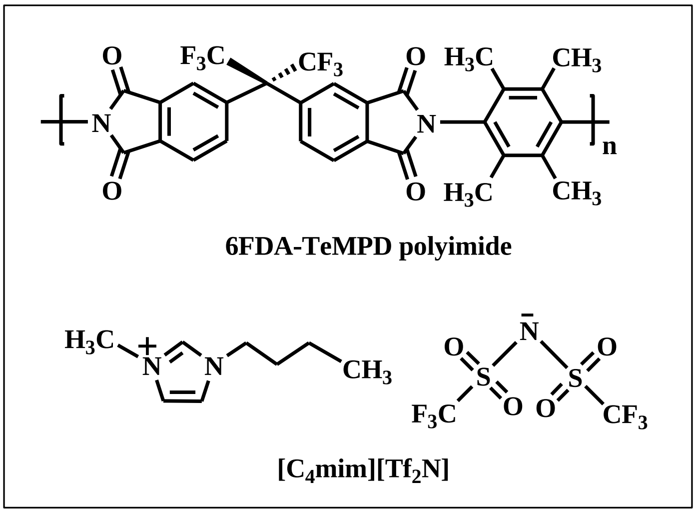

Fig.3A.4: Chemical structures of 4, 4´-(hexafluoroisopropylidene) diphthalicanhydride (6FDA)–2, 3, 5, 6-tetramethyl-1, 4-phenylenediamine (TeMPD) PI and 1-butyl-3-methyl-imidazolium bis(trifluoromethyl-sulfonyl)imide([C_4mim][Tf_2N])

In 2015, Losch *et al.* [78] encapsulated 1-butyl-3-methyl imidazolium methanesulfonate [bmim][CH_3SO_3] ionic liquid on ZSM-5 support by treating tetraethyl orthosilicate (TEOS) as a silicon source and [bmim][CH_3SO_3] as a templating agent resulting in IL/Na-ZSM-5 composite. This composite material was used as solid acid catalyst for chlorination of toluene using trichloroisocyanuric acid.

3A.5 Review of photocatalytic degradation of dyes via advanced oxidation process (AOPs) involving ionic liquid systems

Dye pollution in water

Dye effluents derived from various industries such as leather, paint, textile, printing, paper, rubber, cosmetics, plastic, pharmaceuticals *etc.* are becoming a challenging problem for the environment protection in aquatic region [79, 80]. Annually more than 7 × 10^5 tons of dyes are produced from coal tar and petrochemical intermediates because of the greater demand of the above mentioned industries [81]. Many of the dyes used in different industries are toxic and carcinogenic and thus a risk for living organisms. Ecological and Toxicological Association of Dyestuffs Manufacturing Industry (ETAD) surveyed the toxicity levels of various dyes and observed highest rate of toxicity with diazo, direct and basic dyes [82]. The composite molecular structures of the dyes make them more stable towards light and resistant towards biodegradation [83, 84]. In addition, wastewater from the dye industries possess residual dyestuff, intermediate dyes, and unreacted raw materials like amino compounds, inorganic salts and bases, mineral acids and organic solvents. The presence of such chemicals in water also reduces transmission of sunlight through water and thus decreases the photosynthetic activity of the aquatic plant through lowering of oxygen availability. A small amount of dye (<1 ppm) in water is also highly visible and toxic for the ecosystem. The chemicals in waste water also produce dangerous byproducts through oxidation, hydrolysis, or other chemical reactions. Therefore, different physicochemical processes have been developed for the treatment of colored wastewater such as removal or decolorization and degradation of dyes [81]. Some of these methods are flocculation, precipitation, electro-kinetic coagulation, electro-flotation, membrane filtration, ion exchange, electrochemical destruction, and photo irradiation.

Advanced oxidation process in photocatalytic degradation of dye

The definition of advanced oxidation process represents a set of chemical treatments designed to remove organic chemicals (or inorganic) in water/ or waste water through oxidation reactions involving hydroxyl radicals ($^{\cdot}OH$) [85, 86]. Photocatalysis is one of the advanced oxidation process for degradation of toxic organic chemicals in water under light in presence of photocatalyst. The initiation of photocatalysis proceeds through formation of electron-hole pairs in semiconductor catalysts by absorption of suitable light energy and thus induces chemical reactions of substrate that come in contact with them. Then they undergo regeneration to their initial electronic composition. The AOPs of dye degradation in water requires a high energy light irradiation source (UV light, visible light) and an oxidant to generate hydroxyl radicals to degrade the dyes in waste water [87]. The typical systems include UV/hydrogen peroxide, UV/ozone, UV/Fenton reagent and UV/TiO_2, UV/sunlight or mercury vapour lamp [88-90]. Additionally, an alternative light source, light emitting diodes (LEDs) have also been utilized for the degradation of organic pollutants in water [91, 92].

The degraded dyes undergo mineralization to a large extent into stable inorganic compounds such as water, carbon dioxide and salts. The selections of appropriate semiconductor catalysts with reasonable energy of light for photoactivation are very important to increase the rate of photocatalytic reactions in heterogeneous condition [93]. Photocatalytic reactions may proceed through homogeneously or heterogeneously depending on the state of photocatalysts in contact with other substrate molecules in reaction medium. Out of these two procedures, heterogeneous photocatalysts are extensively employed because the semiconductor catalysts are cheaper, more robust, easily recovered and reusable than the soluble homogeneous photocatalysts. Use of homogeneous photocatalysts has been suffering from various limitations including difficulty in their recovery after the reaction, their photostability and thus resulting possible toxicity.

Necessity of heterogeneous photocatalysis

The primary traditional methods of water treatment such as coagulation, flocculation, filtration, reverse osmosis and adsorption are inefficient to degrade toxic pollutants, but they reduce their concentration levels by converting the pollutants from one form to another and lead to creation of secondary pollutants [81]. Most water soluble non-biodegradable pollutants are resistant to degradation in aerobic treatment. Then, necessity led to uses of advanced oxidation processes for destruction of organic species stable to conventional treatments of waste water. As mentioned in the previous sub-unit, heterogeneous photocatalysis has been proved as AOPs of real interest since they are the efficient tool for degrading both aquatic and atmospheric organic contaminants [94]. It utilizes sunlight, UV light or visible light for excitation of a semiconductor photocatalyst depending on the type of photocatalyst used. Semiconductor photocatalyst accelerates the photoreaction in heterogeneous photocatalysis which involves photocatalytic oxidation to effect partial or total mineralization of gas phase or liquid phase contaminants to benign substances [95]. A well-known and widely used heterogeneous photocatalyst titania (TiO_2) was first revealed as possible water splitting photocatalyst by the pioneering research of Fujishima and Honda [96]. Then extended application of titania dominated the heterogeneous photocatalysis field and has been prevailing its spot as before. Ayodhya *et al.* summarized almost all the reported semiconductor photocatalysts applied till date and mentioned that degradation of the toxic compounds (dyes, pesticides, phenolic compounds *etc.*) using photoactive materials in an aqueous medium mainly depends on the band gap, surface area, amount of catalyst, and generation of an electron-hole pair. High surface area photocatalyst leads to higher adsorption of dye molecule on the surface of heterogeneous photocatalyst and thus speeding up the photocatalytic activity [97]. The authors reviewed a large number of nanostructure semiconductors namely ZnS, CdS, CuS, Ag_2S, Bi_2S_3, CoS, FeS, and PbS in addition to other metal oxide semiconductors including TiO_2, ZnO, WO_3/TiO_2, Nd_2O_3, $Nd_2Sn_2O_7$, $Nd_2Sn_2O_7$-SnO_2, $Nd_2Zr_2O_7$, Ag/CeO_2, Ho_2O_3-SiO_2, Ho_2O_3, $Dy_2Ce_2O_7$, $Dy_2Sn_2O_7$-SnO_2, $CuCr_2O_4$, $Pr_2Ce_2O_7$, $CoO_x/BiVO_4$, Pr_6O_{11}, ZrO_2, Nd_2O_3-SiO_2, $Nd_2Zr_2O_7$-ZrO_2, $Pr_2Zr_2O_7$, and $Cu_2O/TiO_2/Bi_2O_3$ *etc.* as photocatalyst for the degradation of toxic pollutants. As a green and sustainable technology, heterogeneous photocatalysis has been drawing attention while carrying a disadvantage of often phase separation. The concept of an immobilized photocatalyst on an inert support was widely accepted because of its ability to eliminate the costly phase separation processes [98, 99]. This idea led to the synthesis of many excellent photocatalysts anchored onto a variety of surfaces, such as glass, silica gel, metal, ceramics, polymer, thin films, fibres, zeolite, alumina clays, activated carbon, cellulose, reactor walls and others [100]. Thus, heterogenous photocatalysis has become the most useful technique for dye degradation.

Mechanism of photocatalysis

The general mechanism of photocatalytic oxidation of organic pollutant by semiconductor materials involves several steps. This multistep mechanism proceeds by generation of an electron-hole (e^-/h^+) pair in semiconductor particles when radiation energy (hν) is greater or equal to the band gap energy (Eg) of semiconductor. In the process, electrons are excited from the valence band (VB) to the conduction band (CB) of the semiconductor, thus creating an electronic vacancy at the valence band edge which is strongly oxidizing. The conduction band becomes strongly reducing due to the presence of excited electron. Oxidizing ability of a hole induce oxidation of an electron donor while the semiconductor can donate electrons to reduce an electron acceptor thus acts as redox agent depending on the charge transfer to the adsorbed species [101]. **Fig.3A.5** displays the overall mechanism of photocatalytic degradation.

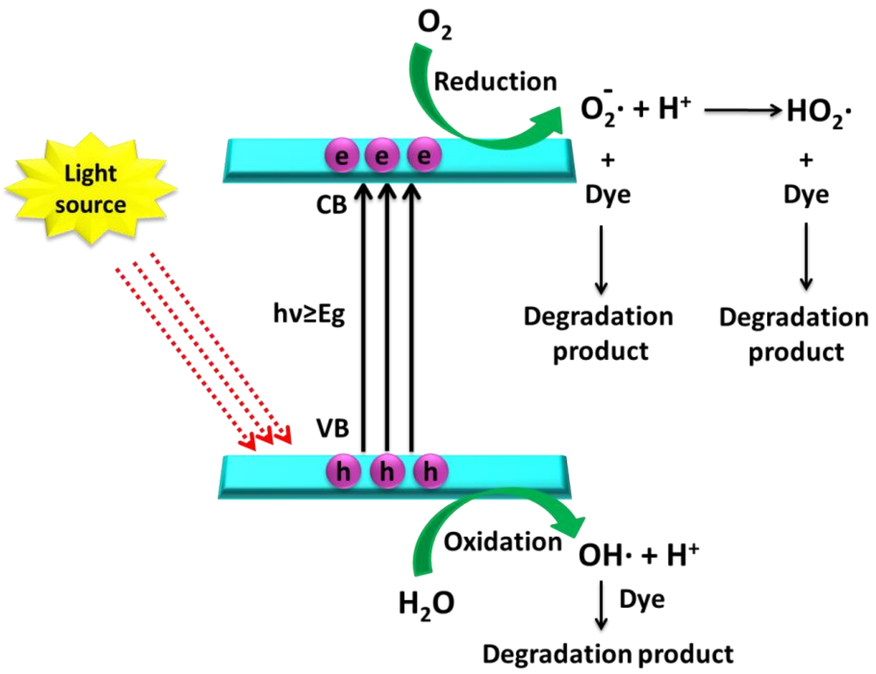

Fig.3A.5: Mechanism of photocatalytic degradation

From the above figure (**Fig.3A.5**) the mechanism can be summarized in five steps: (1) transfer of reactants in the fluid phase to the surface; (2) adsorption of the reactants; (3) reaction in the adsorbed phase; (4) desorption of the products; and (5) removal of products from the interface region [102].

3A.6 Use of ionic liquids in photocatalytic degradation of dyes

Being extensively used in large number of applications, ionic liquids are expanding their region to a higher value. Above section clearly describes the requirement, criteria and necessity of heterogeneous photocatalytic dye degradation methods (**Section 3A.5**). A number of reports explored the effects of ionic liquids as solvent/modifier in metal based photocatalysis for the degradation of dyes under different light sources [103-111].

Hu *et al.* in 2010 synthesized TiO_2 nanocomposites modified with 1-butyl-3-methyl imidazolium hydroxide [bmim][OH] by a hydrothermal procedure. This modification of [bmim][OH] on the surface of TiO_2 particles extended the absorption edge of TiO_2 to visible light region. Electrochemical redox potentials expressed that highest occupied molecular orbital (HOMO) and lowest unoccupied molecular orbital (LUMO) of [bmim][OH] match well with the valence band (VB) and conduction band (CB) of the TiO_2 semiconductor. The ionic liquid is chemically bonded to the surface Ti-OH of TiO_2

particles rather than being adsorbed on the surface thus enhancing the visible light irradiated photocatalytic degradation of methylene blue (**Fig.3A.6**) in aqueous solution [103]. A possible mechanism of electron-hole transition was explained by the authors where the VB and CB were lower in energy than HOMO and LUMO making electron injection from LUMO to CB and electro migration from VB to HOMO possible (**Scheme 3A.6**).

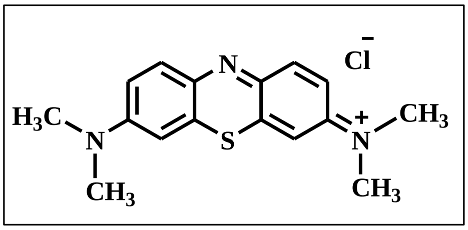

Fig.3A.6: Structure of methylene blue dye

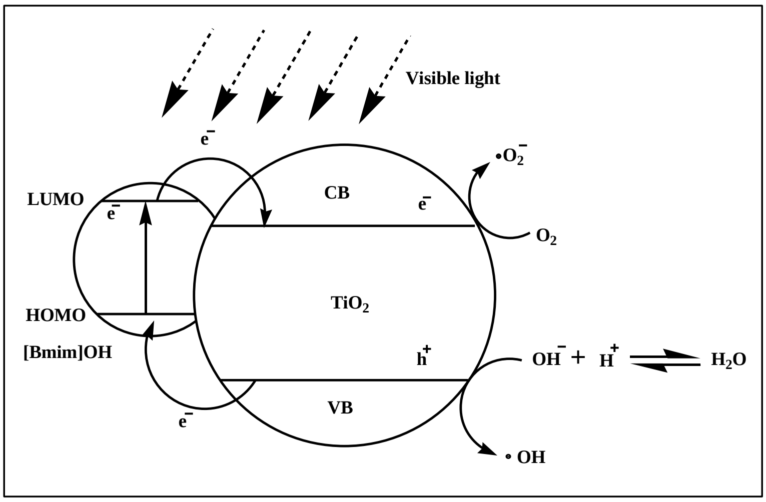

Scheme 3A.6: Photocatalytic degradation mechanism of [bmim][OH]-TiO_2 system

Tao *et al.* (2011) prepared 1-methyl-3-octylimidazolium polyoxomolybdate ionic liquid $[C_8mim]_2[Mo_6O_{19}]$ (C_8mim = 1-methyl-3-octylimidazolium) with low melting point and high stability. They tested photocatalytic performances of the IL *via* degradation of dye rhodamine B (RB) in aqueous solution under the UV light irradiation [104]. Ionic liquid was insoluble in water and acted as an excellent heterogeneous catalyst. Again the same author reported the successful synthesis of the thermally stable polyoxometalate-imidazole ionic liquids (POM-ILs) $[Cnmim]_4[Mo_8O_{26}]$ (Cnmim = 1-alkyl-3-methylimidazolium, n = 12, 14) (**Fig.3A.7**) and efficiently used in UV light induced degradation of rhodamine B (RB) (**Fig.3A.8**) in aqueous solution [105]. The POM-ILs are very stable recyclable heterogeneous catalysts with higher degradation ability.

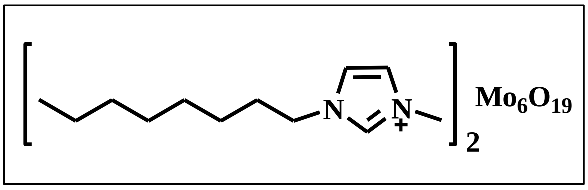

Fig.3A.7: Structure of $[C_8mim]_2[Mo_6O_{19}]$

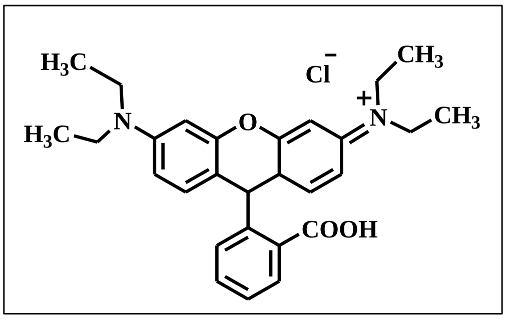

Fig.3A.8: Structure of Rhodamine B

Wang *et al.* (2011) investigated the photocatalysis mechanism of BiOI in detail and developed ionic liquid modified BiOI (IL-BiOI) by *in situ* modification of an ionic liquid [bmim][I] (1-buty-3-methylimidazolium iodide) which significantly enhanced the photocatalytic ability of BiOI. The IL-BiOI was prepared by the reaction of bismuth nitrate with [bmim][I] in water at 70°C, where the ionic liquid could act as both iodine source and surface modified agent. Then they utilized this catalytic system in degradation of methyl orange (MO) under visible light irradiation (λ>420 nm) which proved the superior photocatalytic activity of IL-BiOI photocatalyst than unmodified counterpart synthesized in the absence of [bmim][I]. They proposed that IL modification could trap the photoexcited electron at conduction band of BiOI to inhibit the recombination of photo induced electron-hole pairs and thus trigger its photocatalytic activity (**Scheme 3A.7**) [106].

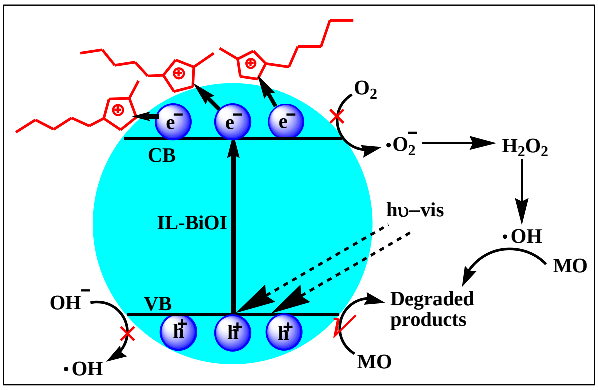

Scheme 3A.7: Mechanistic pathway of MO photodegradation over IL-BiOI

The effects of a room temperature ionic liquid, 1-butyl-3-methylimidazolium terafluoroborate on the photocatalytic performance of Degussa P25 TiO_2 were investigated by Qi *et al.* in degradation of methyl orange (MO) (**Fig.3A.9**) and rhodamine B (RhB). They studied that photogenerated electrons were the main reactive species involved in the photocatalytic degradation of methyl orange (MO), while •OH radicals and photogenerated holes played an important role in the photocatalytic decomposition of rhodamine B (RhB). Addition of ionic liquid slightly enhanced the photodegradtion process in case of MO while suppressed the same in case of RhB [107].

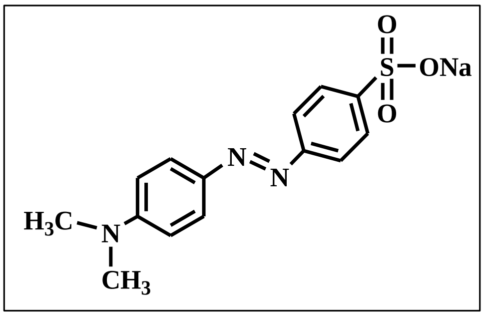

Fig.3A.9: Structure of methyl orange

Synthesis of a copper impregnated titania photocatalyst mesoporous titania (Ms-TiO_2) was assisted by ionic liquid 1-butyl-3-methyl-imidazolium-tetrafluoroborate as a template and an effective additional solvent *via* the sol–gel method at low temperature [108]. The impregnated Cu/Ms-TiO_2 samples bearing several oxygen vacancies exhibit superior visible light photocatalytic activities than that of Ms-TiO_2, P-25 and 2.0% Cu/P-25 in case of 2, 4-dichlorophenol and methyl orange. In this report, ionic liquid was not involved directly as photocatalyst but as template and media for the synthesis of Cu/Ms-TiO_2.

In 2014, Ma and his coworkers synthesized a novel catalytic membrane by grafting a poly(ionic liquid) (PIL) on to polypropylene (PP) membrane followed by ion exchange with polyoxometalate anions (POM) and was successfully employed in degradation of dyes in water under visible light [109]. The membranes PP-g-PVBMC and PP-g-PVBMC-POM were designed by modification of PP nonwoven fabric membrane (PPNWF) using photoinduced grafting of poly(1-(4-vinylbenzyl)-3-methylimidazolium chloride) (PVBMC) and then anchored with phosphomolybdic acid ($H_3PMo_{12}O_{40}$) (**Scheme 3A.8**).

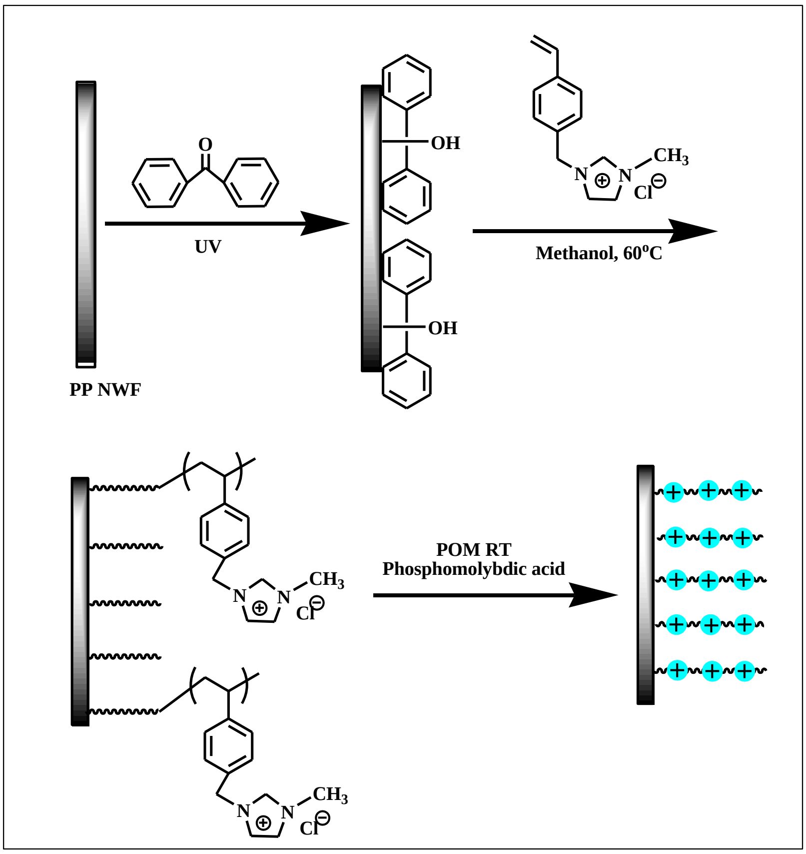

Scheme 3A.8: Synthesis of the catalytic membrane

Photocatalytic activity of the synthesized membranes was evaluated using Acid orange 7 (**Fig.3A.10**) (AO7) as model dye molecule and displayed 95% degradation efficiency.

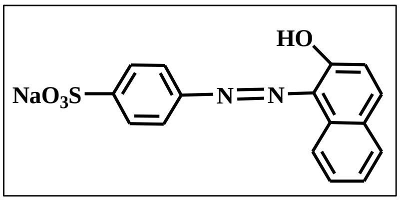

Fig.3A.10: Structure of acid orange 7

Huo and his group (2015) designed a BiOBr visible light photocatalytic films onto a glass substrate by solvothermal process with the assistance of ionic liquid [C_{16}mim][Br] (1-hexadecyl-3-methylimidazolium bromide) which worked as both the bromide source and structure directing agent [110]. This BiOBr films coated on glass substrate enhance the light harvesting due to multiple reflections and thus showed significant photocatalytic ability in visible-light photodegradation of dyeing compounds.

Ji *et al.* (2015) synthesized polymeric ionic liquid (PIL) functionalized Janus nano sheets by polymerization of ionic liquid monomers onto the ATRP (atom transfer radical polymerization) agent modified side of the silica Janus nanosheets in which anion side contained $PW_{12}O_{40}^{3-}$ (**Scheme 3A.9**). They explained excellent photodegradation in water soluble dyes like methyl orange (MO). This heterogeneous system could be regenerated and demonstrated higher degradation at an oil/water emulsion interface [111]. The hydrophobic catalytic intermediate products can be transferred to oil phase and the cooperative procedures can further facilitate the catalytic degradation.

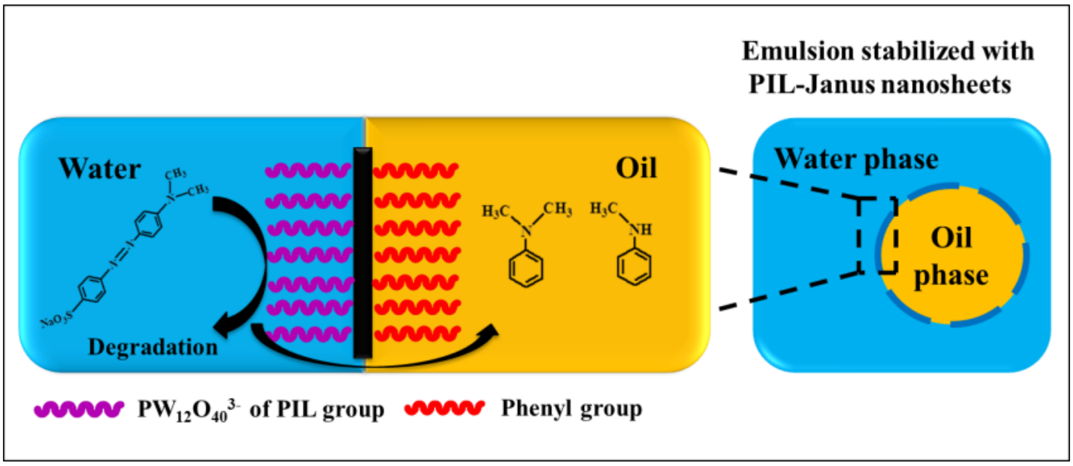

Scheme 3A.9: Schematic illustration of $PW_{12}O_{40}^{3-}$ based PIL Janus nanosheets as a solid surfactant in degradation of MO

In 2015, Wang *et al.* grafted an ionic liquid monomer 1-(*p*-vinylbenzene)-3-methylimidazolium chloride [VBMI][Cl] on the surface of porous silica synthesized by sodium silicate hydrolysis. The porous silica was pretreated with an initiator 2-bromo-2-methyl-N-(3-(triethoxysilyl)propyl)-propanamide (BTPAm) before immobilization of the ionic liquid. Further, Au based catalyst was prepared using chloroauric acid ($HAuCl_4$) and IL-silica hybrid as carrier. The role of this catalyst was to dissociate hydrogen peroxide and produce many hydroxyl radicals which finally destroyed the methyl orange dye in water. The authors described a detailed procedure for the synthesis of Au-hybrid catalyst (**Scheme 3A.10**) [112].

The above literature search clearly reveals that there is no report on the use of halometallate ionic salts or their zeolite supported composite material as semiconductor photocatalysts for the degradation of dyes. The semiconductor nature of 1, 3-disulfoimidazolium chlorometallate of Ni(II) salt $[Dsim]_2[NiCl_4]$ with lower band gap value (2.30 eV) as observed in **Section 2B** (sub-unit **2B.1**) of **Chapter 2** inspired us to design a photocatalytic system consisting of both this semiconductor ionic salt and a porous support like ZSM-5. Despite of the lower band gap value of $-SO_3H$ functionalized $[Dsim]_2[NiCl_4]$ salt, the slight hydrophilic character limits its uses alone as photocatalyst. The immobilization of Ni(II) ionic salt on thermally stable siliceous zeolite ZSM-5 will reduce the moisture sensitive nature of resulting supported materials upon stabilization of active sites of these salts on the surface of ZSM-5 through ionic interactions. In **Section 3B**, we include the synthesis and characterization of one new class of photo-activated HZSM-5 hybrid materials, each of which loaded with five different percentages (3%, 6%, 9%, 17% and 50%) of the Ni(II) ionic salt $[Dsim]_2[NiCl_4]$ on the HZSM-5 support (**Scheme 3A.11**). The prepared supported materials were investigated as possible heterogeneous photocatalysts for decolourizaion of methylene blue (MB) under atmospheric condition involving H_2O_2/sunlight initiated Wet Hydrogen Peroxide Catalytic Oxidation Process (WHPCO) (**Scheme 3A.12**).

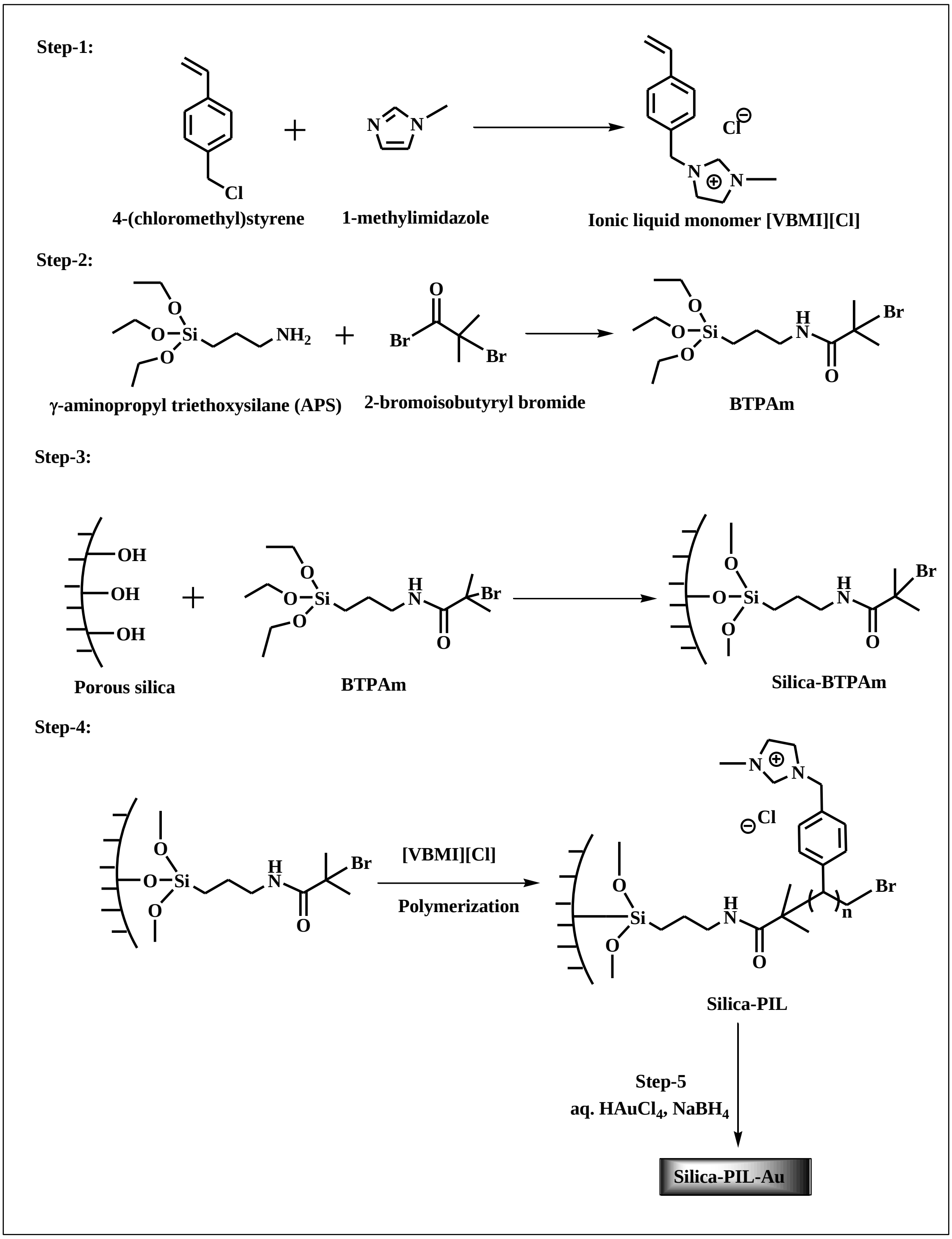

Scheme 3A.10: Stepwise synthesis of Silica-PIL-Au

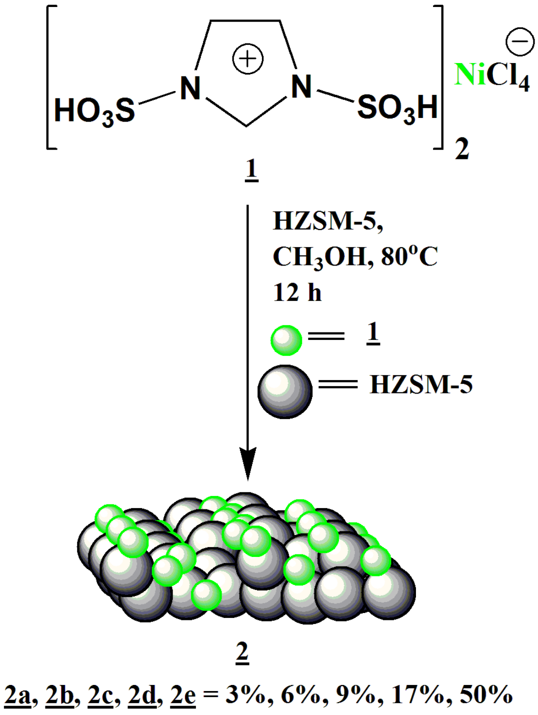

Scheme 3A.11: Preparation of $[Dsim]_2[MCl_4]$/HZSM-5 composites where M = Ni^{+2}

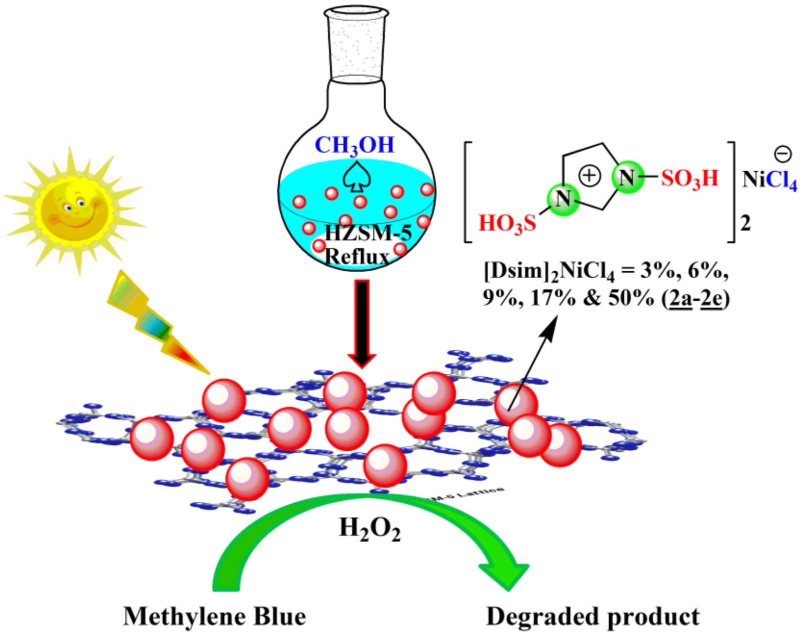

Scheme 3A.12: Method of photocatalytic degradation of methylene blue (MB) using $[Dsim]_2[NiCl_4]$/HZSM-5 composites

3B.1 Characterizations of the composite materials

The preparation of five hybrid samples of 1, 3-disulfoimidazolium chlorometallate of Ni(+2) cation ($[Dsim]_2[NiCl_4]$) with HZSM-5 support (**2a**-**2e**) was done as per the reaction **Scheme 3A.11** using 3%, 6%, 9%, 17% and 50% loading of the ionic salt through wet impregnation method following the general experimental procedure as included in **Experimental Section** (**3B.4**). The ionic salt loaded ($[Dsim]_2[NiCl_4]$)/HZSM-5 supported systems were subjected to analytical characterization using FTIR, UV, SEM-EDX, TEM, PXRD, Raman, BET, TGA, Hammett acidity, photoluminescence and ICP-OES technique *etc.*

FT-IR study

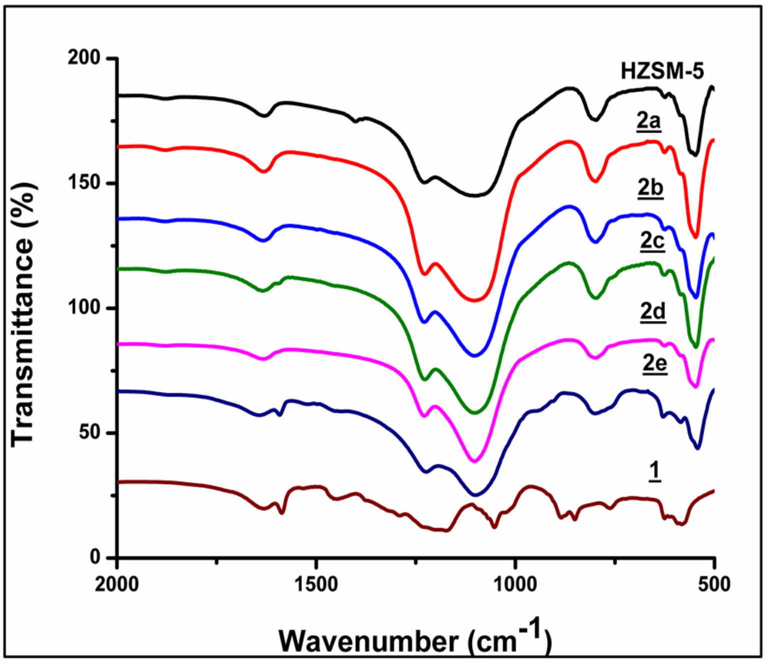

Fig.3B.1: IR spectra of **1**/HZSM-5 (**2a**-**2e**)

FT-IR spectra in **Fig.3B.1** showed characteristic bending and stretching vibration of zeolite framework and crystalline phases of the hybrid samples of Ni(+2). The fundamental external symmetric and internal asymmetric stretching vibrations of T-O-T linkage (T = Si or Al) of zeolite structure are displayed at 797-801 cm^{-1} as weak band and around 1106-1230 cm^{-1} as strong band respectively [113]. As compared to the parent HZSM-5 spectra, narrowing of the T-O asymmetric and widening of the external symmetric band occurred up to **2d**. Additionally, the asymmetric T-O stretching band is also overlapped with the asymmetric stretching vibration of –SO_3H group at 1075 cm^{-1} [114]. The external linkages between TO_4 units in HZSM-5 structure can be confirmed from external asymmetric stretching band [115] at 1226-1230 cm^{-1} and this is merged at 1222 cm^{-1} for S-O symmetric stretch of -SO_3H. The double five ring lattice vibration of MFI type zeolite is seen at 543-553 cm^{-1} [116]. An absorption peak at 450 cm^{-1} can be assigned for T-O bending vibrations of the SiO_4 and AlO_4 internal tetrahedron. The characteristic crystalline structure of HZSM-5 is also displayed from the two absorptions at 543 and 450 cm^{-1} [117]. Later on the ratio of intensities of these two peaks were used for estimation of the degree of crystallinity of modified HZSM-5 samples (**Table 3B.1** and **Fig.3B.2**). These ratios were observed in the range of 0.77-0.81 for the hybrid samples (**2a**-**2d**), which was reported as 0.8 for the parent HZSM-5 zeolite [115, 118]. The retention of crystalline structure of the modified $[Dsim]_2NiCl_4$/HZSM-5 systems were further confirmed in PXRD analysis (**Fig.3B.5**) up to 50% ionic salt loaded sample **2e**. The IR absorbance spectra in **Fig.3B.2** represents silicate vibrations of HZSM-5 and five compositions of **1**/HZSM-5 (**2a**-**2e**) hybrid materials and this stipulates the existence of indigenous crystallinity of parent HZSM-5 in **2a**-**2d**. The relative percentage crystallinity data calculated from the PXRD analysis also (**Table 3B.2**) clearly expressed that **2e** lost its crystallinity up to almost 20%. On the other hand, other hybrid materials showed gradual loss in their crystallinity as compared to HZSM-5. The optical density ratio of **2e** included in **Table 3B.1** is also excluded from the values in between 0.75-0.85 while remaining four hybrid systems up to **2d** are included in this range which denotes the crystalline nature of the materials. The maximum optical density value 1.01 of highest loaded sample (**2e**) beyond 0.85 confirms the significant loss of crystalline nature as compared to the parent HZSM-5. The absorption peak at 1630 cm^{-1} is assigned as bending vibration of adsorbed water on HZSM-5 support and also this peak position is merged with C=N stretching vibration of imidazolium cation [119]. The IR pattern of the 50 % loaded sample (**2e**) have additional peak at 1592 cm^{-1} for Ni(+2) system in addition to maximum destruction of the external symmetric stretch vibrations around 797-801 cm^{-1}.

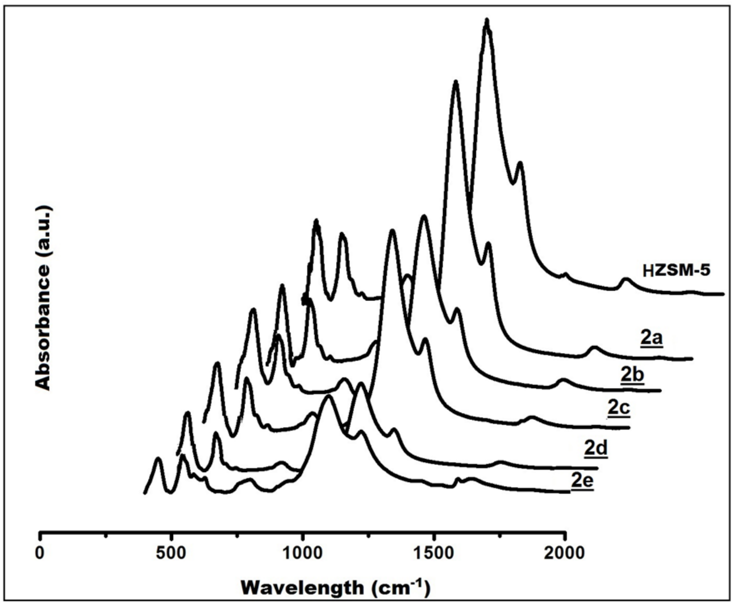

Fig.3B.2: IR absorbance spectra of **1**/HZSM-5 (**2a**-**2e)** with respect to parent HZSM-5 for optical density calculation

Table 3B.1: Optical density calculation from IR absorbance spectra

Entry	Optical density ratio					
	HZSM-5	**2a**	**2b**	**2c**	**2d**	**2e**
1/HZSM-5	0.83	0.81	0.79	0.79	0.77	1.01

Optical density ratio=Absorbance at 556 cm^{-1}/Absorbance at 450 cm^{-1}

These investigations support the intactness of HZSM-5 structure within the modified framework of hybrid zeolite materials (**2a**, **2b**, **2c** and **2d**). To confirm the destruction of highest loaded sample (**2e**), the O-H stretching vibration of hybrid samples and HZSM-5 were analyzed within frequency range 3000-3800 cm^{-1} in **Fig.3B.3**. Two O-H stretching vibrations are found for parent HZSM-5 in the **Fig.3B.3** at 3662 cm^{-1} as weak absorption attached to extraframework aluminium (EFAl) species and at 3452 cm^{-1} as broad band for Si-OH groups of hydroxyl nests within the zeolite framework [114].

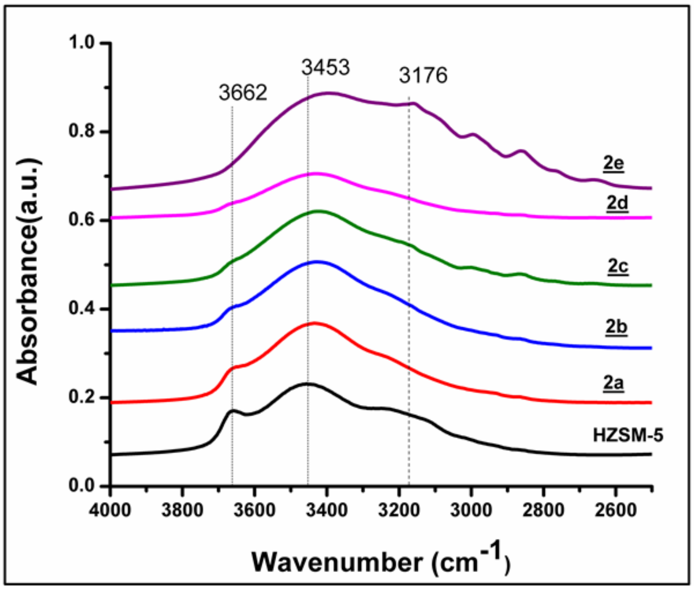

Fig.3B.3: O-H stretching vibrations of **1**/HZSM-5 (**2a**-**2e**)

This can be described as outcome of thermal initiated removal of some tetrahedral framework Al into EFAl species in siliceous ammoniated ZSM-5 zeolites at 500°C during conversion to acidic HZSM-5 for 5-6 hour [47]. The ionic salt supported composition of HZSM-5 displays reinsertion of the EFAl species into the zeolite structure as framework Al which is supported by reduction of absorption peak intensity at 3662 cm^{-1} with increasing loading up to the 17% of ionic salt. The peak maximum of silanol group of hydroxyl nests at 3453 cm^{-1} shift towards 3610 cm^{-1} as broad absorption and this can be accounted for the framework Al with increasing loading of the ionic salt (**Fig.3B.3**) [120]. The phonomenon of acid mediated realumination of EFAl in dealuminated HZSM-5 was first explored by Fan *et al.* using citric acid on HZSM-5 zeolites, initially dealuminated by steaming [47]. The structure modification of HZSM-5 zeolites *via* realumination of the extraframework aluminium species will produce more number of Brönsted acidic sites on the surface of modified composition of zeolites and their presence can be observed from UV-Vis Hammett plots in **Fig.3B.11**. **Fig.3B.3** also shows few additional absorbance in between 2800-3200 cm^{-1} for the highest loaded sample **2e**. The appearance of more absorption peak in this region can be described for alkali mediated desilication of the highly siliceous HZSM-5 structures in case of the 50% ionic salt loaded composition **2e** [121]. The desilication of zeolite framework may occur upon *in situ* formation of metal hydroxide of Ni(+2) from water sensitive chlorometallate during the synthesis of **2e**. Therefore, we get comparable thermal stabilities of the **2e** with the pure ionic salt (**1**) in thermogravimetric (TGA) analysis (**Fig.3B.4**).

Thermogravimetric analysis

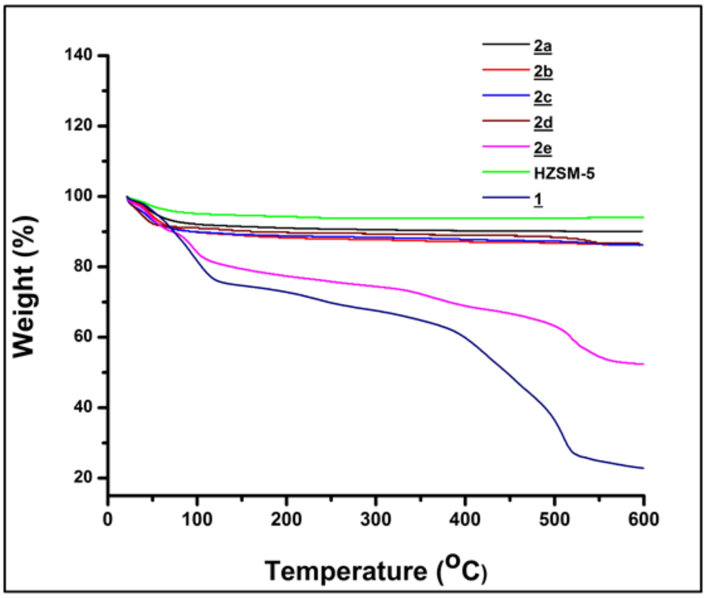

Fig.3B.4: TGA graph of **1**/HZSM-5 (**2a**-**2e**) with respect to parent HZSM-5

The TGA patterns of the hybrid series (**2a** to **2d**) represents elimination of 5-8% loss of adsorbed water below 100°C (**Fig.3B.4**). As compared to the parent HZSM-5, the modified series become more hygroscopic with rising amount of Brönsted-Lewis acidic ionic salt $[Dsim]_2NiCl_4$. The thermal degradation profile of **2e** becomes identical with the pure ionic salt (**1**). This decomposition process of **2e** can be accounted for the desilication of HZSM-5 structure as discussed in the IR study (**Fig.3B.3**) [122]. Each of the hybrid system, (**2a** to **2d**) has comparable thermal stability with the HZSM-5 profile (up to 600°C).

Powder XRD analysis

The powder X-ray diffraction analysis expressed identical patterns for the hybrid series of zeolites (**2a**-**2d**) similar to that of basic HZSM-5 zeolite (**Fig.3B.5**) with increasing amount of the ionic salt up to 17% loading on the zeolite support. Above that in case of the **2e**, it displayed distinct reduction of peak intensity at 2θ = 7.78, 23.07, 45.1. This PXRD analysis evidences the existence of crystalline zeolite with the MFI topology for the supported materials **2a**-**2d** [123, 124]. No other characteristic peaks are found for the ionic salt.

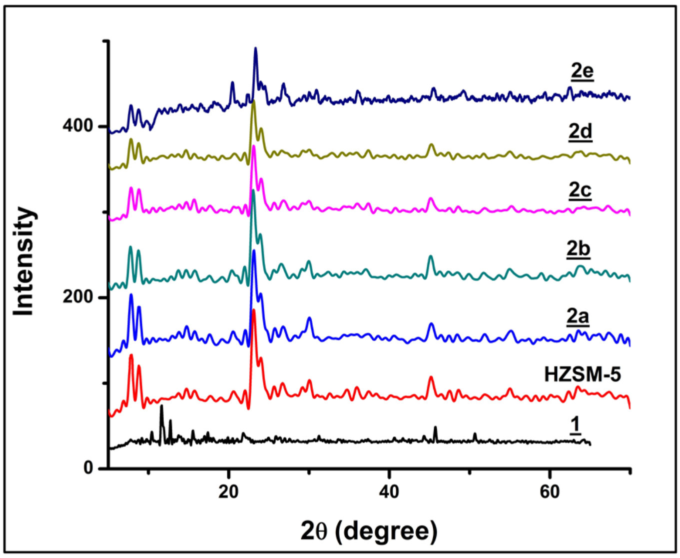

Fig.3B.5: PXRD pattern of **1**/HZSM-5 (**2a**-**2e**) with respect to parent HZSM-5

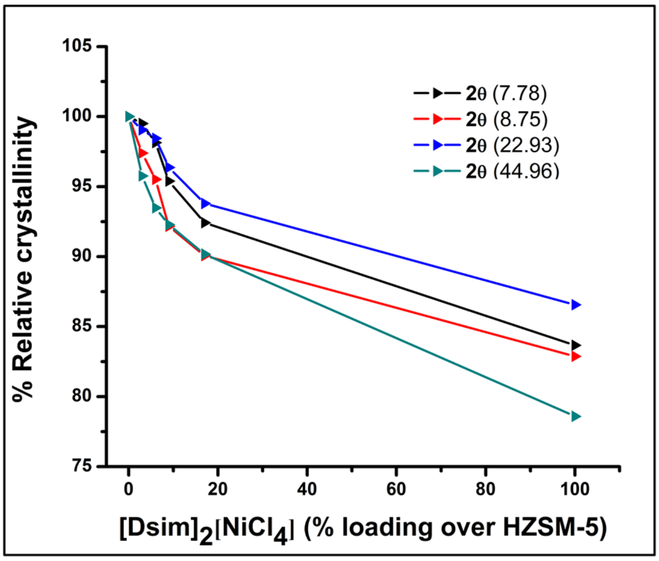

Fig.3B.6: Percentage crystallinity graph of **1**/HZSM-5 (**2a**-**2e**) with respect to parent HZSM-5

Fig.3B.6 plots the percentage crystallinity for four intense peaks of the modified hybrid series in the region of 2θ = 8-45^{o} with reference to the parent HZSM-5 and their values are mentioned in the **Table 3B.2**. These values express gradual loss of crystallinity of the ionic salt modified HZSM-5 compositions up to **2d**. Beyond that the 50% loaded hybrid sample **2e** shows maximum loss of crystallinity because of maximum hygroscopic nature of the supported material and thus destruction of the HZSM-5 network structure occurs as evidenced from the **Fig.3B.3** of O-H stretch and the **Fig.3B.4** of TGA profile.

Table 3B.2: Relative % crystallinity table for the hybrid materials

2θ (degree)	Relative % crystallinity					
	HZSM-5	**2a**	**2b**	**2c**	**2d**	**2e**
7.78	100	99.50	98.14	95.39	92.42	83.67
8.75	100	97.39	95.52	92.16	90.07	82.87
22.93	100	99.05	98.45	96.37	93.79	86.56
44.96	100	95.76	93.48	92.28	90.18	78.59

Raman spectra

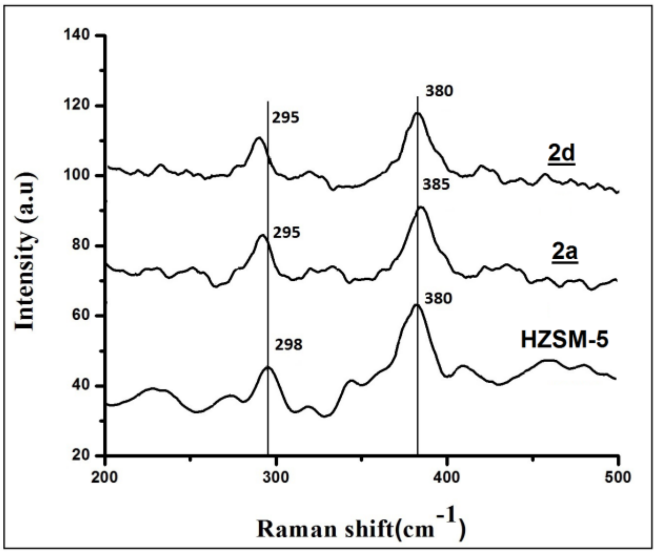

Fig.3B.7: Raman spectra of **1**/HZSM-5 (**2a** & **2d**) with respect to parent HZSM-5

Only two systems of IL/HZSM-5 composites namely **2a** and **2d** were used to study the influence of chlorometallate on the framework of HZSM-5 using an excitation laser beam of 514 nm. The well-defined bands of Ni(+2) based ionic salt in **Fig.3B.7** are attributed to symmetric stretching vibrations of Si-O-Si bonds of five-membered silicate framework of MFI unit structure along with other characteristic peaks at 290, 380, 460 cm^{-1} [125]. The basic peak value of the parent HZSM-5 at 298 cm^{-1} is slightly shifted its position to 295 cm^{-1} in the modified systems of Ni(+2) ionic salt. The other characteristic peak at 460 cm^{-1} is also broadened with reduction of peak intensity. This Raman analysis also displays absence of any additional peaks for the hybrid material up to **2d** which supports the preservation of the MFI topology in these hybrid materials without inclusion of the Ni(+2) cation into the tetrahedral framework of zeolite.

SEM analysis

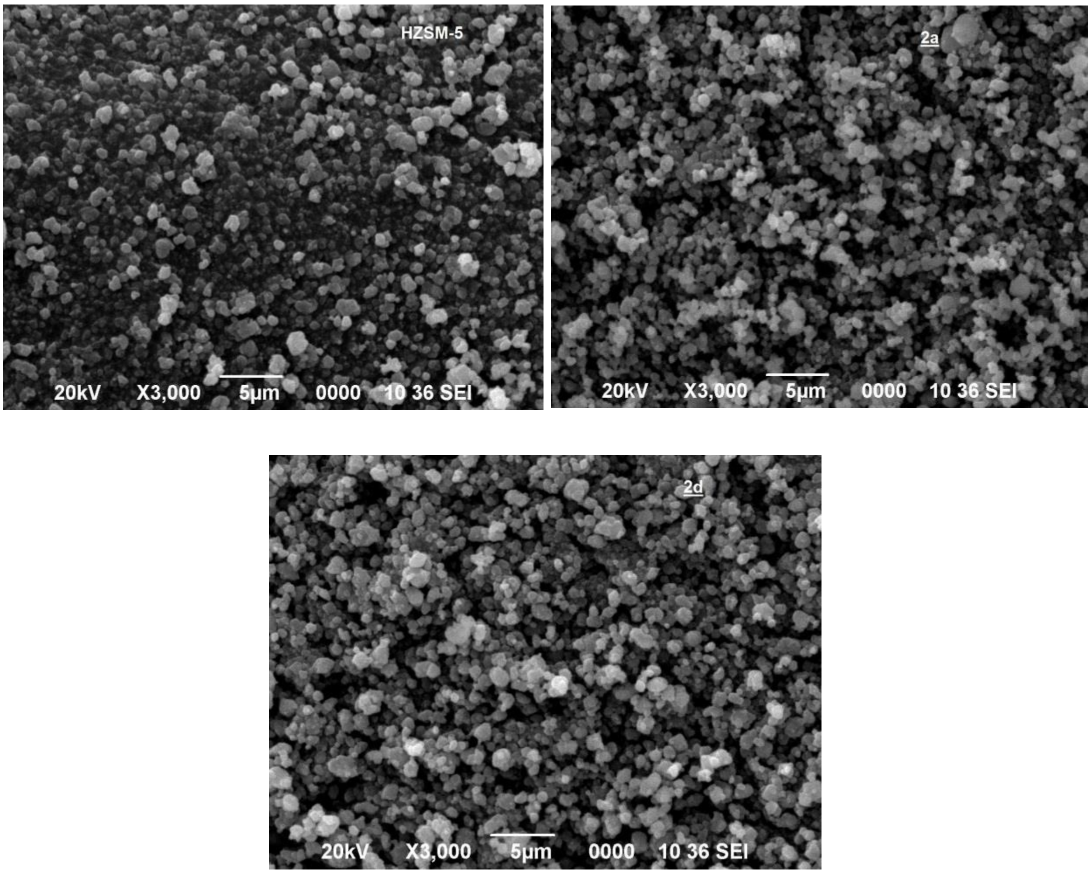

Fig.3B.8: SEM images of **2a**, **2d** & HZSM-5

SEM images of **2a** and **2d** hybrid systems were taken to assess the reliability of PXRD data and confirm the surface topology of IL/HZSM-5 compositions with respect to the HZSM-5 in **Fig.3B.8**. The image of **2a** containing lowest loading of the ionic salt reflects starting of clustering and aggregation of small crystallite particles to a lesser extent without appreciable change of their sizes and shapes. The formation of more clusters on the surface of 17% loaded system **2d** can be accounted for involvement of H-bonding interaction of new Brönsted acidic sites of the framework Al regenerated from reinsertion of the EFAl species to the HZSM-5 framework as explained in the study of O-H stretching vibration modes (**Fig.3B.3**). This observation is also confirmed from the estimation of relative crystallinity data of hybrid series obtained in the **Table 3B.1** and **Table 3B.2**.

EDX analysis

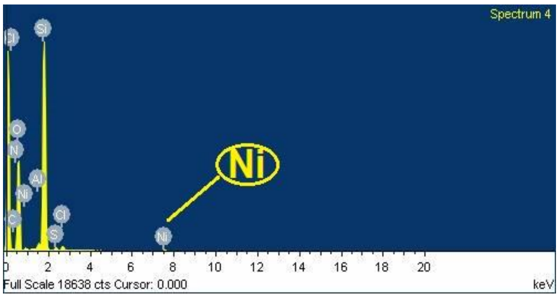

Fig.3B.9: EDX images of $[Dsim]_2[NiCl_4]$/HZSM-5 composite **<u>2d</u>**

Fig.3B.9 for energy dispersion X-ray analysis of **<u>2d</u>** supports the retention of metal precursor Ni(+2) in $[Dsim]_2[NiCl_4]$/HZSM-5 material in addition to other necessary elements of the zeolite structure such as Al, Si and O.

TEM analysis

The low resolution TEM image of **<u>2d</u>** (17% loaded) confirms aggregation of the modified HZSM-5 hybrid sample. The high resolution TEM (HRTEM) images of **<u>2a</u>** (3%), **<u>2d</u>** (17%) and HZSM-5 samples in **Fig.3B.10** also evidence for existence of cluster formation on the surface of modified HZSM-5 with increasing amount of the $[Dsim]_2[NiCl_4]$ ionic salt.

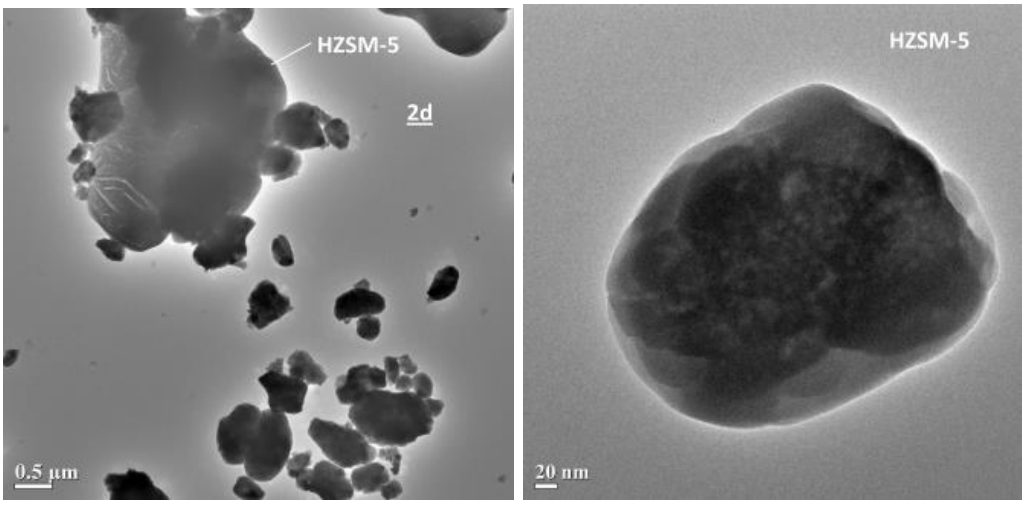

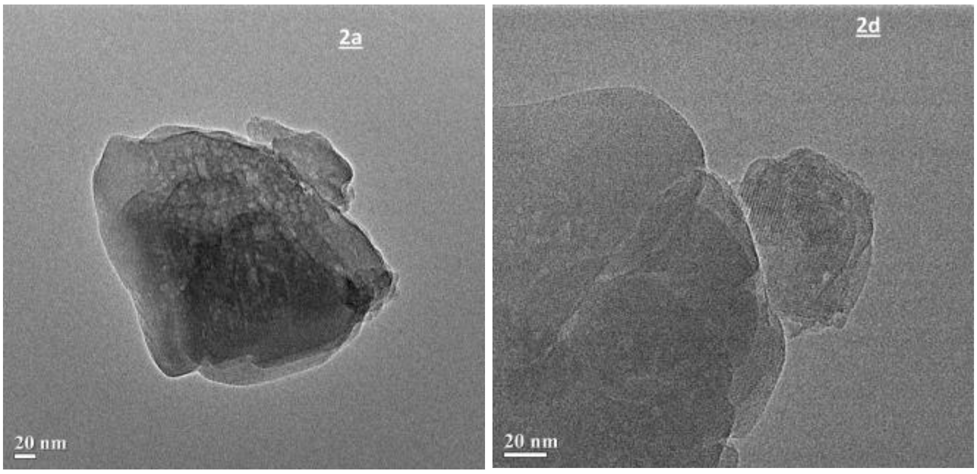

Fig.3B.10: Low resolution TEM image of **2d** at 0.5µm & high resolution TEM images of HZSM-5, **2a** and **2d** at 20 nm

Hammett acidity determination by UV-Visible

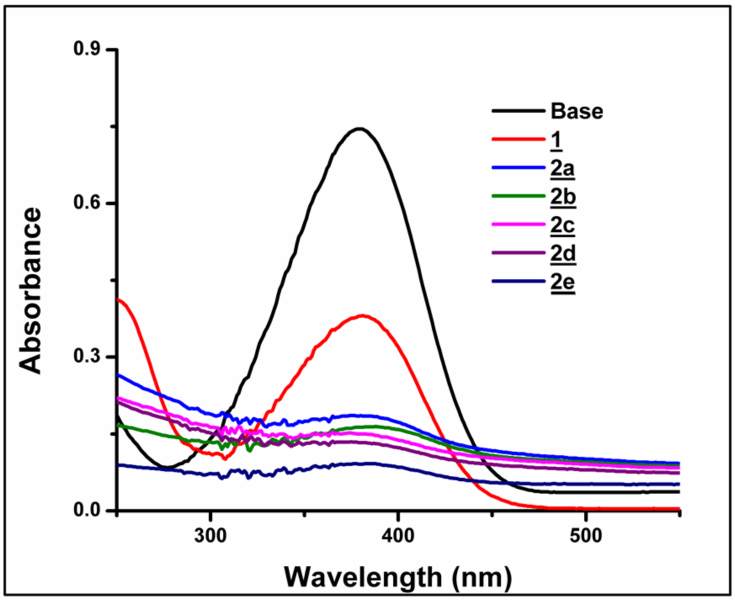

Fig.3B.11: Hammett plot of **1**/HZSM-5 in ethanol

In section **2B.1 Characterization of the catalyst** of **Chapter 2** we have already discussed the detail procedure involved in quantitative Hammett acidity measurement of acidic material. From the Hammett plot (**Fig.3B.11**), the acidity of all these hybrid systems can be ordered with reference to the parent ionic salt as: **2e**>**2d**>**2c**>**2b**>**2a**>**1**. This increasing trend of Brönsted acidic sites from lower to higher loading of the acidic ionic salt **1** on HZSM-5 support can be accounted for realumination of the thermal initiated EFAl species of the basic HZSM-5 framework to framework Al-OH in modified materials. The realumination process occurs due to treatment of the basic dealuminated HZSM-5 with various percentages of the acidic ionic salt of Ni^{+2} as indicated from variation of two types of O-H stretching vibrations of the zeolites discussed from the **Fig.3B.3 [**114**]**. **Table 3B.3** indicates the Hammett acidity values of the analyzed hybrid systems and thus describe the lost in absorption intensity towards the highest loaded samples.

Table 3B.3: Hammett acidity values of the hybrid materials of $[Dsim]_2[NiCl_4]$/HZSM-5

Entry	**A_{max}**	**[I]%**	**$[IH^+]$%**	**H^o**
Base	0.745	100	0	-
1	0.380	51.00	49.00	1.01
2a	0.187	25.10	74.90	0.51
2b	0.166	22.28	77.72	0.44
2c	0.152	20.40	79.60	0.39
2d	0.131	17.58	82.42	0.32
2e	0.094	12.61	87.39	0.15

UV-Visible diffuse reflectance spectra

The UV/Vis diffuse reflectance spectra of four hybrid compositions of $[Dsim]_2[NiCl_4]$/HZSM-5 were examined in **Fig.3B.12**. A distinct small shoulder at 267 nm is assigned as ligand to metal charge transfer transition of tetrahedral Ni(+2) complex [119]. The lower intensity hump at 510 nm and another peak around 345 nm of **2d** spectra could be attributed to d-d transition of either extraframework Ni(+2) or surface immobilized $[Dsim]_2[NiCl_4]$ chlorometallates in tetrahedral co-ordination environment [126]. Also they describe the effects of HZSM-5 support on the absorption peaks of immobilized ionic salt (**1**). The **Fig.3B.12** also shows weak to broad absorption bands near 267, 345 and 510 nm in **2a**-**2d** for Ni(+2) present in $[Dsim]_2[NiCl_4]$/HZSM-5.

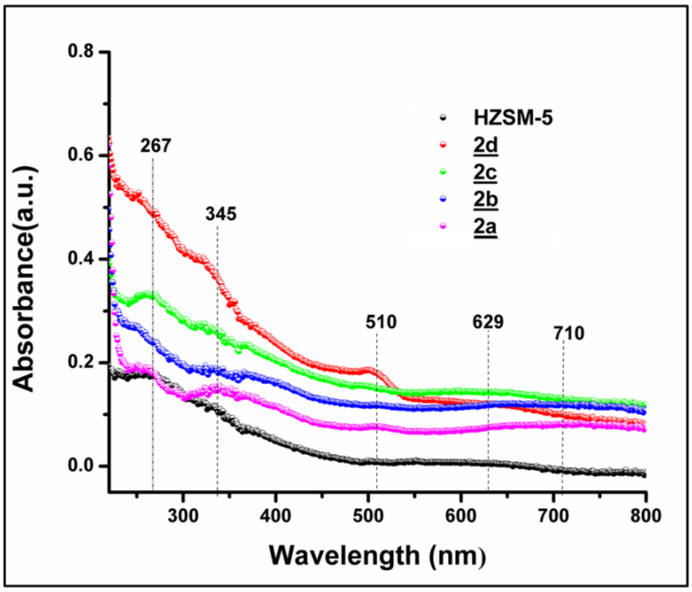

Fig.3B.12: UV-Visible DRS spectra of **1**/HZSM-5 (**2a**-**2d**) and HZSM-5

BET analysis:

N_2-adsorption-desorption isotherms

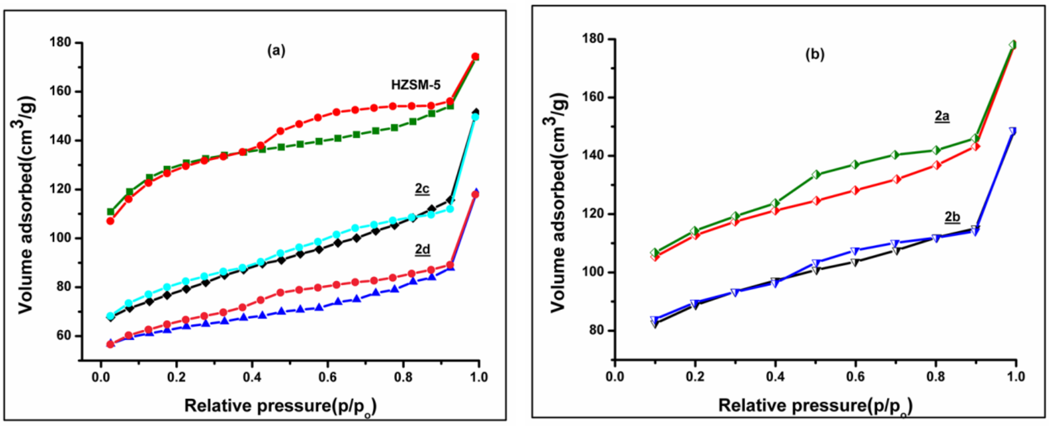

Fig.3B.13: N_2-isotherm of (a) HZSM-5, **2c** and **2d** (b) **2a** and **2b**

To study the textural properties of ionic salt inserted HZSM-5 composites BET analysis was performed. The isotherms in **Fig.3B.13 (a)** & **(b)** are characteristic of combined **type I** and **type IV** isotherms with type-H4 hysteresis loop (according to IUPAC classification), which expresses the formation of a hierarchical porous system with the HZSM-5 framework containing both micropores and mesopores. At initial lower pressure region, a sharp increase in adsorbed volume occurs due to the filling of micropores. After that, there is a clear increase of N_2 adsorption in $0.4<P/P_0<0.95$ region, which is interpreted as capillary condensation in inter/intracrystalline mesopore void spaces present in the initially dealuminated HZSM-5 and composite materials [127-129]. The contribution of both micropores and mesopores to overall porosity (total pore volume) of the material become significant. Hysteresis loop of **2d** was remained same even after the incorporation of chlorometallate of Ni(+2) ionic salt.

BJH pore size distribution

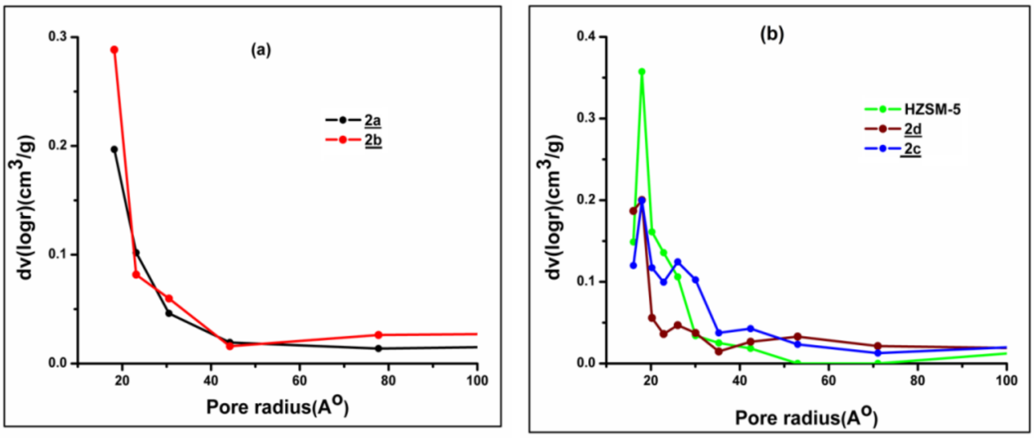

Fig.3B.14: BJH plots of **2a**-**2d** and HZSM-5

Fig.3B.14 displays the BJH pore size distribution plot of the basic HZSM-5 with the ionic salt supported HZSM-5 systems using only adsorption branch of the isotherm. The mean size of micropores in HZSM-5 and loaded composites was calculated to be about 17.99A^{o}-18.15A^{o} (1.79-1.81 nm).

t-Plot method

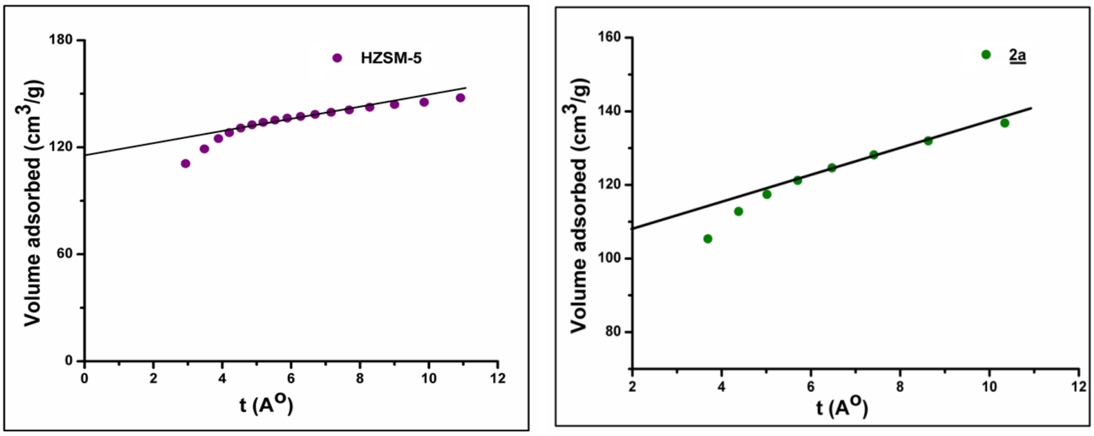

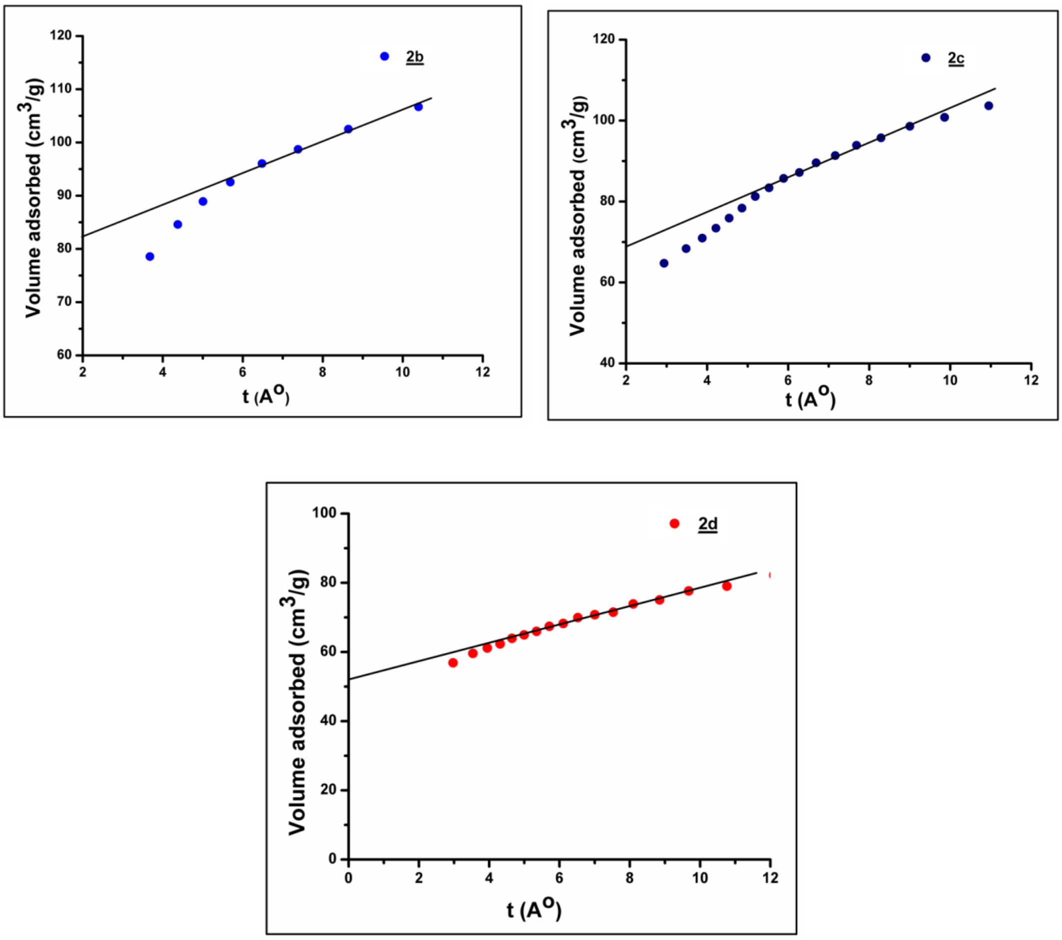

Fig.3B.15: t-plots of HZSM-5, **2a**-**2d**

The adsorption isotherms of the hybrid materials were transformed into t-plots (**Fig.3B.15**) by conversion of relative pressures (p/p_o) into t values using **Equation 3B.1** as follows which was given by De Boer [130].

$$t\ (A^o) = [13.99/(\log(p_o/p) + 0.034)]^{0.5} \qquad \textbf{(Equation 3B.1)}$$

The pore volume was obtained from the positive intercept of the straight line through t-plot data with the y-axis (V_{MP} = i*.001547cm^3). External crystal surface areas and mesoporous areas are calculated from the slopes of straight lines through the respective t-plot data in **Fig.3B.15** [A ($m^2\ g^{-1}$) = slope* 15.47].

The analyzed BET surface area (S_{BET}), external surface area (S_{EXT}), micropore volumes (V_{mp}) data are summarized in **Table 3B.4**. This table indicates that the BET surface area of the modified samples decreases with increase in chlorometallate loading on the HZSM-5 support. This can be explained as a result of decrease in porosity during loading leading to decrease in the surface area. This continuity was also similar in case of the micropore volume.

Table 3B.4: Summary of BET analysis

Entry	$S_{BET}{}^{a}$ (m^2/g)	$S_{EXT}{}^{b}$ (m^2/g)	$V_{mp}{}^{b}$ (cm^3/g)	$S_{mp}{}^{c}$ (m^2/g)
HZSM-5	428.77	53.34	0.17	375.43
2a	337.71	49.57	0.16	288.14
2b	223.87	39.21	0.13	184.66
2c	223.37	45.93	0.10	177.44
2d	171.10	36.09	0.081	135.01

[a] Surface area calculated form multipoint BET; [b] External surface areas and micropore volumes are measured by t-plot method; [c] $S_{mp} = S_{BET} - S_{EXT}$

Investigation of photocatalytic ability using emission spectra

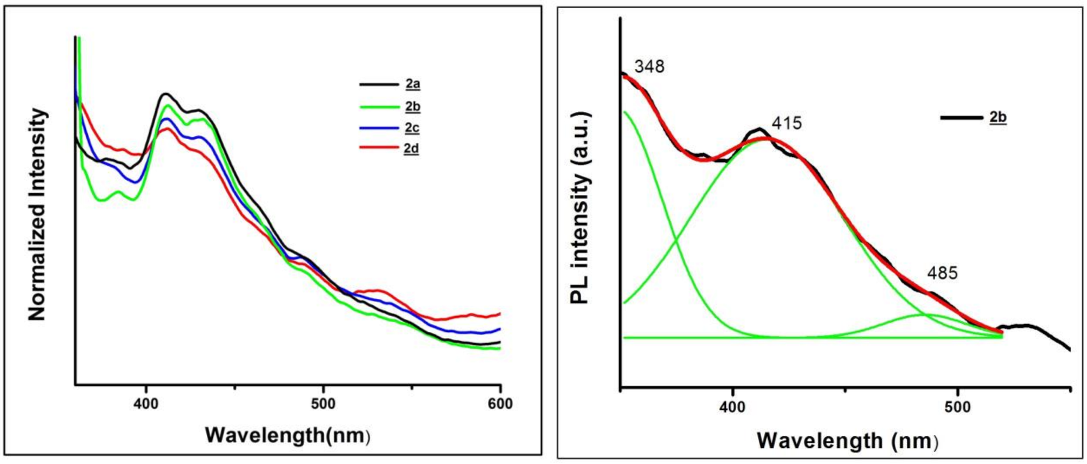

(a) (b)

Fig.3B.16: (a) Photoluminescence emission spectra of **1**/HZSM-5 (**2a**-**2d**) & (b) Gaussian fitting curves of **2b**

Photoluminescence (PL) spectra of the synthesized chlorometallate anchored HZSM-5 materials were recorded to assess their optical properties at excitation wavelength of 330 nm in **Fig.3B.16(a)**. These PL emission spectra covered wide wavelength range from 350 to 600 nm. This emission spectra for chloronickellate confined HZSM-5 seemed to be made up of more than one Gaussian peaks. For all the samples, there was no considerable shift of peak positions of the emission spectra. Therefore, we considered to resolve one spectrum of **Fig.3B.16(a)** to identify the peak positions centered at 348, 415 and 485 nm in **Fig.3B.16(b)**. The variation of peak intensity of PL spectra of four hybrid systems can be reasoned as the creation of various level of defective sites within the framework of highly siliceous HZSM-5 zeolite after treatment with the acidic chlorometallate salt of Ni(+2). The peak intensity of PL spectra slowly reduced as the amount of ionic salt increases from **2a** to **2d** that may lead to the lowest recombination rate of excited electron and hole pairs in the higher loaded material [131, 132]. The generation of extraframework Al species in HZSM-5 structure by thermal treatment before immobilization of the ionic salt can create sufficient number of defective sites at hybrid material with low loading which may prefer the possible electron hole recombination rate. Again the realumination of EFAl to these defective sites of zeolite was occurred in **2b**-**2d** (6%-17%) and thus may lead to blocking of the electron-hole recombination process. The material possessed lower electron-hole recombination could be used as efficient heterogeneous photocatalyst for degradation of dye molecules with excess number of photo-excited electrons [133].

3B.2 Photo catalytic performance study for advanced oxidative degradation of methylene blue

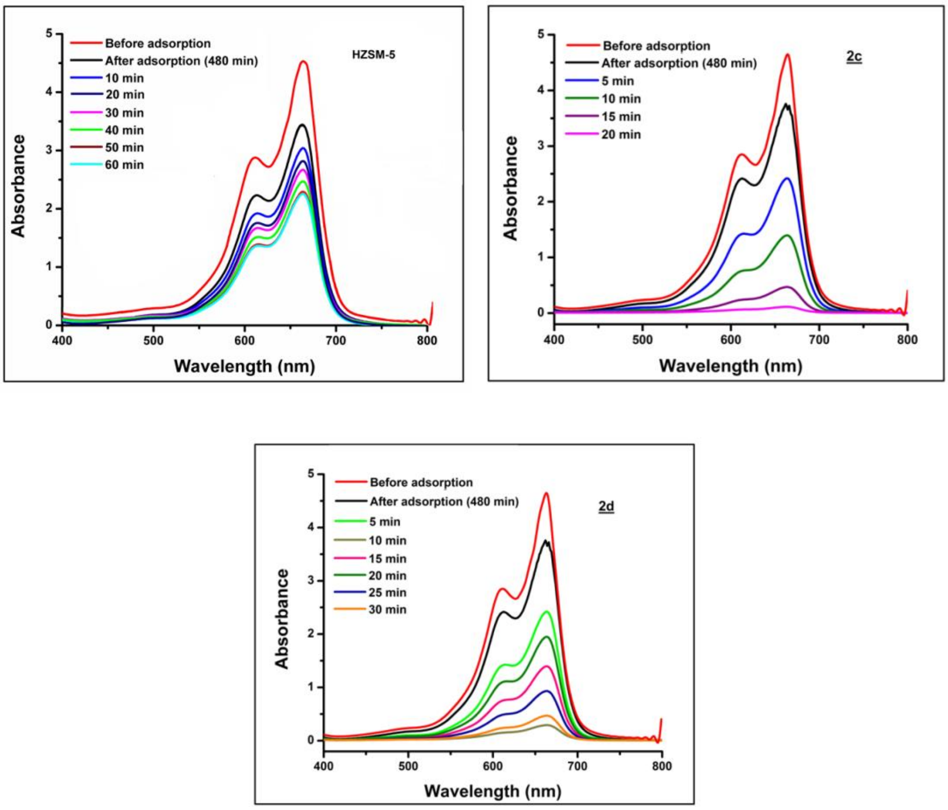

Fig.3B.17: UV-Visible analysis of MB dye degradation using HZSM-5, **2c** and **2d**

The wet H_2O_2 catalytic oxidation (WHPCO) method was used to investigate the degradation rate of the model dye methylene blue (MB) in water containing **2c**/**2d** or parent HZSM-5 as heterogeneous photocatalyst under sunlight irradiation as observed from time dependent UV-Vis spectra in **Fig.3B.17**. The assessment of catalytic performance of **2a** and **2b** were avoided. Since, they have lower efficiency as photocatalysts than that of **2c** and **2d** which can be explained from the photoluminescence spectra (**Fig.3B.16**). Initially, the adsorption equilibrium was achieved before irradiation by stirring 50 mg of catalyst (**2c** or **2d**) in 100 ml of MB solution (100mg/L) for 8 hour in dark condition at ambient temperature and then followed by addition of 100 μL of 30% H_2O_2 under sunlight. This method decomposes the dye up to 92-97% after irradiation within 20-30 min for the two catalysts. For the degradation of MB, higher dye degradation rate was observed for the catalyst **2c** as compared to **2d** (**Fig.3B.17**). The reactive hydroxyl radical generated from H_2O_2 involved in redox reaction of Ni(+2) to Ni(+3) of the ionic salt on zeolite framework can be reasoned as the increased rate of degradation of adsorbed MB dye. The lower activity of **2d** as photocatalyst can be co-related to non-availability of active sites for adsorption of large number of the MB molecules in presence of greater number of clusters of the ionic salt attached to the zeolite surface which was already evidenced from the SEM images (**Fig.3B.8**).

The degradation rate (%) of dye molecule was determined using **Equation 3B.2** and plotted with reaction time in **Fig.3B.18(a)** (**Table 3B.5**).

$$\text{Degradation rate (\%)} = (A_0 - A_t)/A_0 \times 100 \qquad \textbf{(Equation 3B.2)}$$

Where A_0 is the initial absorbance of MB solution after kept it in adsorption equilibrium for 480 min in presence of catalyst before addition of H_2O_2 and A_t is the absorbance at a given reaction time ‘t’ for MB solution at wavelength 664 nm.

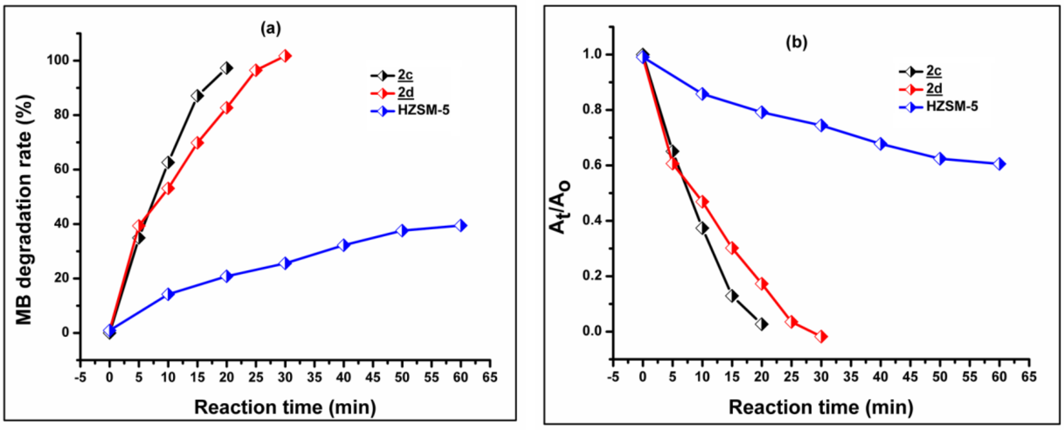

Fig.3B.18: (a) Plot of degradation rates (%) of MB with respect to reaction time for **2c**, **2d** and HZSM-5 (b) Plot of A_t/A_0 versus irradiation time

Table 3B.5: MB dye degradation rate (%) with reaction time

Reaction time (min)	Degradation rate (%)^{a,b} = $(A_0\text{-}A_t/A_0)*100$			
	2c		**2d**	
	A_t	(%)	A_t	(%)
5	2.42	35	2.41	35
10	1.39	63	1.94	48
15	0.48	87	1.37	63
20	0.10	97	0.93	75
25	-	-	0.46	88
30	-	-	0.28	92

[a] Degradation rate (%) were calculated using A_0 =3.72, [b] All the degradation rates are taken as approximate percentage values.

The plots of A_t/A_0 versus irradiation time displayed linear change of dye concentration after degradation in **Fig.3B.18(b)** (for same wavelength and concentration $C_1/C_2 = A_1/A_2$) [134]. **Fig.3B.19** represents the plots of Ln (A_t/A_0) versus t (sunlight irradiation time) for the two catalysts. The graphs display a linear trend which further correlates the graph in **Fig.3B.18(b)** suggesting an exponential relation observed for pseudo 1st order reaction kinetics at minimum dye concentration (Ln $(A_t/A_0) = -kt$, where k is the apparent rate constant in min^{-1}). The graphs clearly justify the identical relationship as seen in

Fig.3B.17 and **Fig.3B.18**. The slope derived from linear fit regression plots of two catalysts provided us with the value of photodegradation reaction constants for each case. Additionally, the correlation coefficient values (R^2 ~ 0.91-0.97) of the two catalysts indicated that the dye degradation reaction followed pseudo first order kinetics [135]. Thus, it was further proved that the catalyst **2c** having large rate constant (k = 0.17) is more efficient than **2d** (k = 0.08) for the photodegradation of MB.

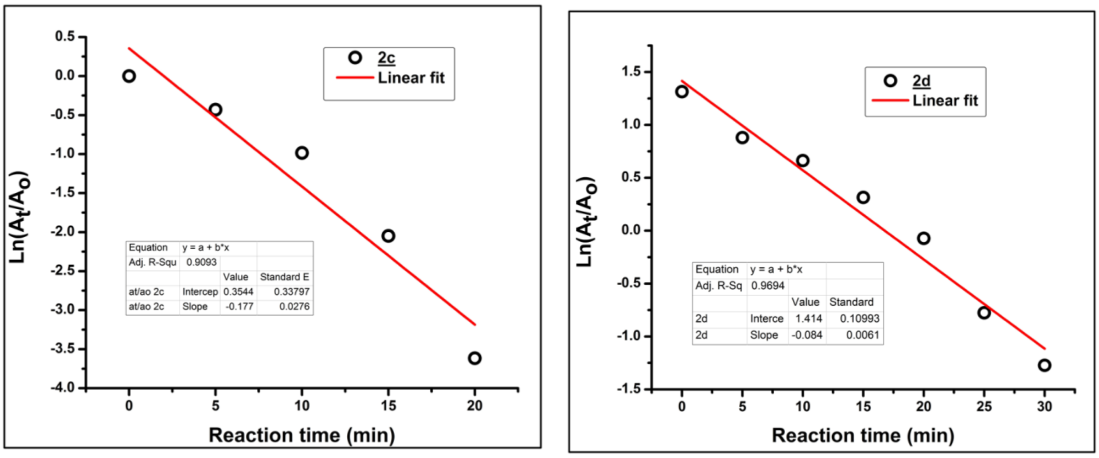

Fig.3B.19: 1st order regression plots of MB dye degradation

Furthermore, **Fig.3B.20** represents that the use of 20 mg of catalyst **2c** was not enough for degradation of 100 ml of MB solution (100 mg/L) by following the optimized procedure as discussed in experimental section. This amount of catalyst can degrade the MB dye up to 81% within 30 min of reaction.

The involvement of •OH radical as a reactive oxidizing species was proved using 2-propanol as hydroxyl radical scavenger. The photo degradation rate was drastically reduced [136].

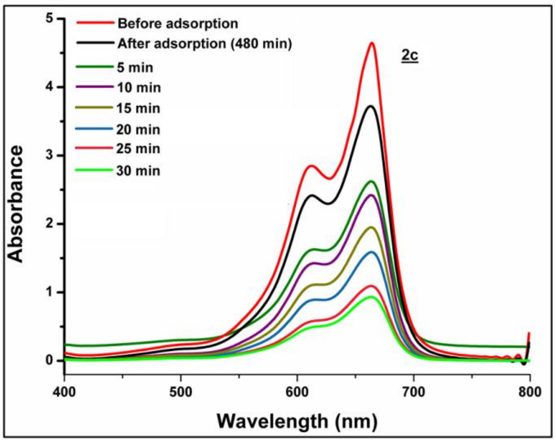

Fig.3B.20: MB degradation using 20 mg of **2c**

Mechanism of MB degradation

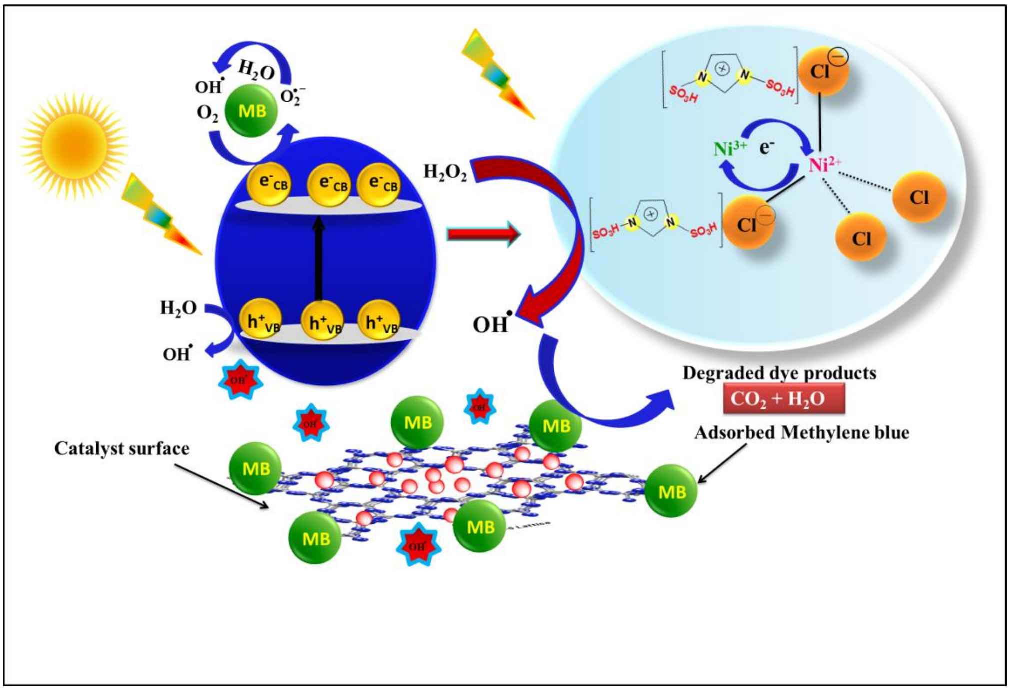

Fig.3B.21: Schematic representation of methylene blue degradation

The probable mechanism of oxidative degradation may occur through transfer of photoactivated electron from immobilized halogenated organocatalyst $[Dsim]_2[NiCl_4]$/HZSM-5 to hydrogen peroxide for *in situ* generation of highly reactive hydroxyl radical (•OH) as oxidizing species for degradation of the adsorbed MB on catalyst surface (**Fig.3B.21**). It was found in literature that chlorination of conjugated system is a practical route for designing of n-type organic semiconductor material [137]. In this way, the band gap of conjugated moiety can be significantly reduced *via* delocalization of π-electron over vacant d-orbital of halogens due to -I inductive effect which can be expected to cause absorption in visible region [138]. Here, the imidazolium bridged chloride ligand of tetrahedral complex anion $[NiCl_4]^{2-}$ of the ionic salt can accomplish the electron transport process between the oxidation state of Ni(+2) to Ni(+3) involving H_2O_2/ sunlight system.

Determination of total organic carbon (TOC)

This experiment demonstrated TOC removal rate of 9% (**<u>2c</u>**) and 17% (**<u>2d</u>**) in **Fig.3B.22** along with HZSM-5 [139]. Interestingly, the TOC removal efficiencies of **<u>2c</u>** and **<u>2d</u>** follow the similar trend in terms of mineralization as indicated in the **Fig.3B.17**, **3B.18** & **3B.19**.

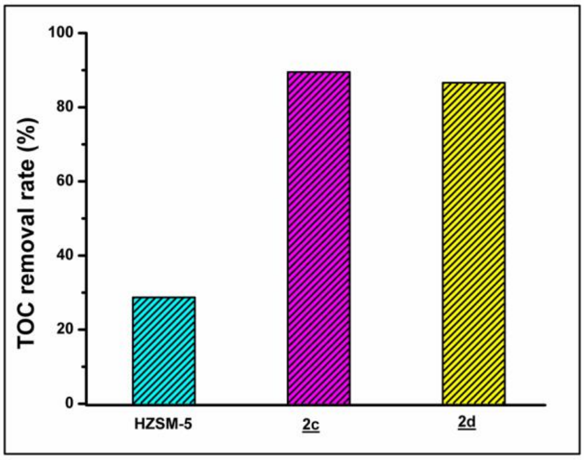

Fig.3B.22: TOC removal percentage of **2c** and **2d** with respect to HZSM-5

Evidence of degradation and mineralization process

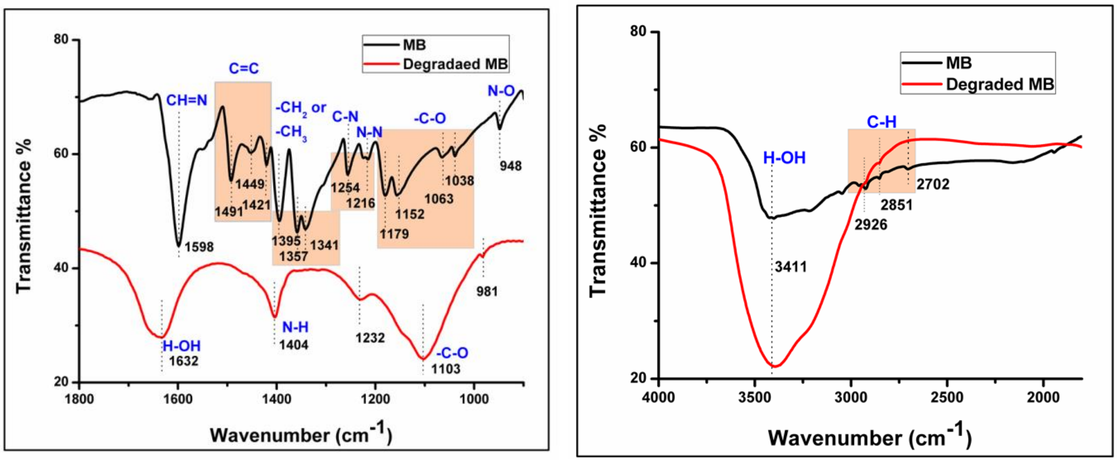

Fig.3B.23: FTIR spectra of methylene blue (MB) before degradation and after degradation

This study was conducted by comparing the IR spectrum of degraded MB product with the non-degraded dye sample (**Fig.3B.23**). The characteristic IR peaks of MB were disappeared from finger-print region at 1598, 1421-1491, 1341-1395, 1216, 1254, 1038-1179, 948 cm^{-1} in the spectrum of degraded MB product (**Fig.3B.23**). Also the aromatic C-H stretch around 2702-2926 cm^{-1} was absent in the degraded MB spectrum. The complete change of these IR peaks for the degraded MB evidenced the existence of mineralized products indicating the complete photodegradation process [132, 140].

Catalyst recyclability study

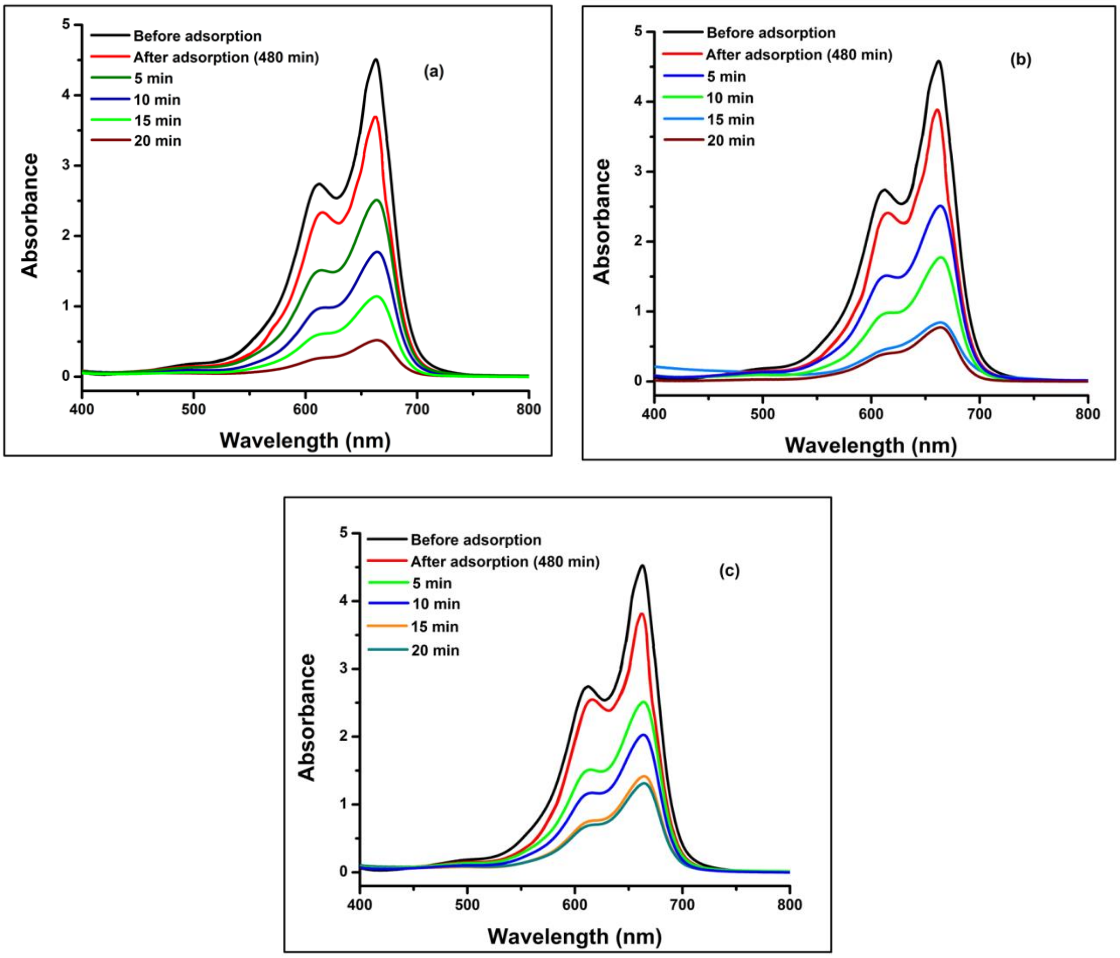

Fig.3B.24: UV-visible analysis of MB dye degradation by recycled catalyst **2c**

Table 3B.6: Calculation of degradation rate (%) of methylene blue for recycled catalyst

Entry	**2c**[a]	
	A_t	%
1st recycle	0.47	87
2nd recycle	0.78	79
3rd recycle	1.35	65

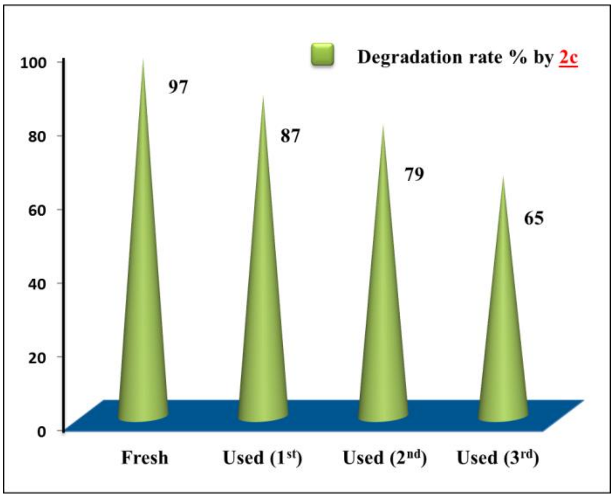

Fig.3B.25: Dye degradation rate (%) of **2c** for four consecutive cycles

The reusability of catalyst was evaluated only for the **2c** (50 mg) up to 20 min reaction time (**Fig.3B.24**). The recycled catalyst **2c** displayed gradual loss of catalytic activity in **Fig.3B.25** with 65% degradation of the MB after three consecutive uses (**Table 3B.6**). This can be reasoned for slow hydrolysis of the loaded $[Dsim]_2[NiCl_4]$ salt into metal hydroxide in aqueous solution for longer reaction time (~8.6-35 h). This type of hydrolysis reaction was earlier observed with the degradation pattern of **2e** in the thermogravimetric analysis (**Fig.3B.4**). The IR spectrum of spent catalyst also expressed increasing sharpness of bending vibration of adsorbed water around 1630 cm^{-1} on the HZSM-5 surface as compared to the fresh catalyst **2c** (**Fig.3B.26(a)**). The identical PXRD pattern of reused catalyst with the fresh catalyst was observed due to higher degree of crystallinity of siliceous HZSM-5 (**Fig.3B.26(b)**).

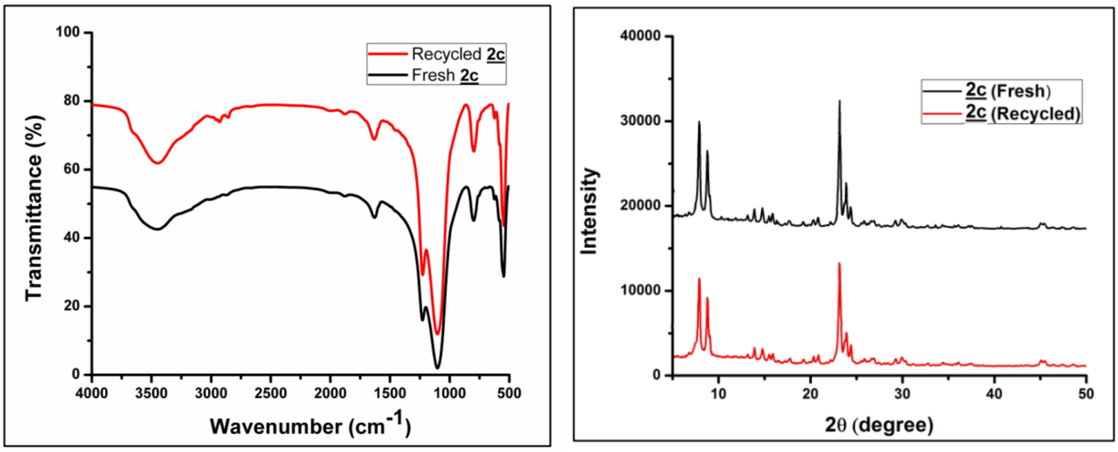

(a) (b)

Fig.3B.26: (a) FTIR spectra & (b) PXRD pattern of **2c** (recycled) with the fresh **2c**

3B.3 Conclusion

Here, we studied the structural modification of parent HZSM-5 zeolite *via* dealumination of framework Al during thermal treatment of ammoniated HZSM-5 followed by reinsertion of the EFAl to the zeolite frame after immobilization of various percentage of semiconductor organometallic salt 1, 3-disulfoimidazolium chloronickellate on the HZSM-5 support as $[Dsim]_2[NiCl_4]$/HZSM-5. The various compositions of ionic salt modified HZSM-5 systems were completely characterized using various analytical techniques. The thermal analysis of hybrid materials showed comparable thermal stabilities with the parent HZSM-5 and also minimum amount of physisorbed water up to 17% loading of the ionic salt. Observed destruction of the HZSM-5 framework for 50% loaded system near 100^oC can be accounted for *in situ* generation of metal hydroxide from hygroscopic ionic salts and then alkali initiated desilication of siliceous zeolite structure as proved from the IR and PXRD crystallinity analyses [31]. The modified less hygroscopic and thermally stable two materials **2c** and **2d** were successfully examined as possible heterogeneous catalyst for photocatalytic degradation of MB dye using H_2O_2/ sunlight involved advanced oxidation process. The bridging chloride ligand containing imidazolium-chloronickellate complex induced photoexcitation of electrons in the catalytic system and hence brought feasibility to the hybrid catalyst by accomplishing the electron transfer which briskly initiated the photodegradation process in presence of H_2O_2 under visible light. This approach offers a new insight to semiconductor chlorometallate modified porous photocatalyst with enormous possibility in various aspects.

3B.4 Experimental section

General techniques

Ammoniated HZSM-5 powders and other necessary chemicals were purchased from ACROS Chemicals. The acidic ionic salt 1, 3-disulfoimidazolium tetrachloronickellate $[Dsim]_2[NiCl_4]$ was prepared following the previous reported method [119]. The same instruments as mentioned in **Section 2B** of **Chapter 2** (**2B.4 Experimental section**) were utilized for IR, TGA, UV/Vis diffuse reflectance spectra, SEM-EDX, Raman, PXRD, and UV-Vis Hammett acidity studies. Additionally, BET isotherms were recorded on QUANTACHROME, NOVA 1000E surface pore size analyzer and photoluminescence spectra were taken using DELVAC (LYODEL) fluorescence spectrophotometer. HRTEM images were taken from Transmission Electron Microscope JEOL-2100. TOC-Analyzer

(Model No.: Aurora 1030 C; Make: M/s O.I. Analytical, USA) was used to analyze total Organic Carbon (TOC).

Procedure for synthesis of 1, 3-disulfoimidazolium tetrachloronickellate supported HZSM-5 material [Dsim]$_2$[NiCl$_4$]/HZSM-5

The ammoniated HZSM-5 powder with Si/Al = 80 was degassed for 5-6 h in a muffle furnace at 550^{o}C. The degassed sample was collected as HZSM-5 after removal of NH_3 during degassing. Then the ionic salt $[Dsim]_2[NiCl_4]$ loaded HZSM-5 materials were prepared in five different w/w ratios (**2a**, **2b**, **2c**, **2d** and **2e**) by stirring calculated amount of solid ionic salts in methanol and HZSM-5 powder at 80^{o}C under reflux for 12 hour. Methanol solvent was evaporated under reduce pressure in rotary evaporator and the prepared solid materials were further dried in vacuum at 100^{o}C for 3-4 h.

Method for photocatalytic degradation MB dyes

Before irradiation, 50 mg of each catalyst (**2c** and **2d**) and 100 ml of MB solution (100 mg/L) was stirred at atmospheric temperature under dark condition in a 250 mL two necked round bottom flask for 8 hour to reach an equilibrated adsorption. To the reaction mixture, then 30% H_2O_2 (100 μL) solution was added to complete the oxidative degradation process of dye molecule under direct sunlight irradiation. A certain amount of sample solution was collected at periodic intervals from the centrifuged reaction mixture and the concentration of organics was determined by UV-Vis spectrophotometer at room temperature.

References

1. Scott, J., Guang, D., Naeramitmarnsuk, K., Thabuot, M. and Amal, R. Zeolite synthesis from coal fly ash for the removal of lead ions from aqueous solution. *Journal of Chemical Technology & Biotechnology: International Research in Process, Environmental & Clean Technology*, 77(1):63-69, 2002.
2. Rayalu, S., Meshram, S. U. and Hasan, M. Z. Highly crystalline faujasitic zeolites from flyash. *Journal of Hazardous Materials*, 77(1-3):123-131, 2000.
3. Murayama, N., Yamamoto, H. and Shibata, J. Mechanism of zeolite synthesis from coal fly ash by alkali hydrothermal reaction. *International Journal of Mineral Processing*, 64(1):1-17, 2002.
4. Auerbach, S. M., Carrado, K. A. and Dutta, P. K. *Handbook of zeolite science and technology*. CRC Press, New York, 2003.

5. Jha, B. and Singh, D. N. A review on synthesis, characterization and industrial applications of flyash zeolites. *Journal of Materials Education*, 33(1):65-132, 2011.
6. Jha, B. and Singh, D. N. Zeolitization characteristics of fly ashes from wet and dry disposal systems. *Acta Geotechnica Slovenica*, 9(2):63-71, 2012.
7. Loewenstein, W. The distribution of aluminum in the tetrahedra of silicates and aluminates. *American Mineralogist: Journal of Earth and Planetary Materials*, 39(1-2):92-96, 1954.
8. Rüscher, C. H., Salman, N., Buhl, J. C. and Lutz, W. Relation between growth-size and chemical composition of X and Y type zeolites. *Microporous and Mesoporous materials*, 1(92):309-311, 2006.
9. Gottardi, G. The crystal chemistry of natural zeolites. *Pure and Applied Chemistry*, 58(10):1343-1349, 1986.
10. Müller, M., Harvey, G. and Prins, R. Comparison of the dealumination of zeolites beta, mordenite, ZSM-5 and ferrierite by thermal treatment, leaching with oxalic acid and treatment with $SiCl_4$ by ^{1}H, ^{29}Si and ^{27}Al MAS NMR. *Microporous and Mesoporous Materials*, 34(2):135-147, 2000.
11. Jha B., Singh D. N. Basics of Zeolites. *In: Fly Ash Zeolites. Advanced Structured Materials*, Springer, Singapore, 2016.
12. Čejka, J. and van Bekkum, H. *Zeolites and ordered mesoporous materials: progress and prospects.* The 1st FEZA School on Zeolites, Prague, Czech Republic, volume 157, Gulf Professional Publishing, 2005.
13. Widayat, W. and Annisa, A. N. Synthesis and characterization of zsm-5 catalyst at different temperatures. In *IOP Conference Series: Materials Science and Engineering* volume 214, pages 012032, IOP publishing, 2017.
14. Hay, D. G., Jaeger, H. and West, G. W. Examination of the monoclinic / orthorhombic transition in silicalite using XRD and silicon NMR. *The Journal of Physical Chemistry,* 89(7):1070-1072, 1985.
15. Grau-Crespo, R., Acuay, E. and Ruiz-Salvador, A. R. A free energy minimisation study of the monoclinic-orthorhombic transition in MFI zeolite. *Chemical Communications*, 21:2544-2545, 2002.

16. Lónyi, F. and Lunsford, J. H. The development of strong acidity in hexafluorosilicate-modified Y-type zeolites. *Journal of Catalysis*, 136(2):566-577, 1992.
17. Triantafillidis, C. S. and Evmiridis, N. P. Dealuminated H-Y zeolites: influence of the number and type of acid sites on the catalytic activity for isopropanol dehydration. *Industrial & Engineering Chemistry Research*, 39(9):3233-3240, 2000.
18. Han, S., Shihabi, D. S. and Chang, C. D. Selective removal of surface acidity in ZSM-5 zeolite using (NH_4) $2SiF_6$ treatment. *Journal of Catalysis*, 196(2):375-378, 2000.
19. Apelian, M. R., Fung, A. S., Kennedy, G. J. and Degnan, T. F. Dealumination of zeolite β via dicarboxylic acid treatment. *The Journal of Physical Chemistry*, 100(41):16577-16583, 1996.
20. Yan, Z., Ma, D., Zhuang, J., Liu, X., Liu, X., Han, X., Bao, X., Chang, F., Xu, L. and Liu, Z. On the acid-dealumination of USY zeolite: A solid state NMR investigation. *Journal of Molecular Catalysis A: Chemical*, 194(1-2):153-167, 2003.
21. Knözinger, H. and Huber, S. IR spectroscopy of small and weakly interacting molecular probes for acidic and basic zeolites. *Journal of the Chemical Society, Faraday Transactions*, 94(15):2047-2059, 1998.
22. Kustov, L. M., Kazanskii, V. B., Beran, S., Kubelkova, L. and Jiru, P. Adsorption of carbon monoxide on ZSM-5 zeolites: Infrared spectroscopic study and quantum-chemical calculations. *Journal of Physical Chemistry*, 91(20):5247-5251, 1987.
23. Zecchina, A. and Areán, C. O. Diatomic molecular probes for mid-IR studies of zeolites. *Chemical Society Reviews*, 25(3):187-197, 1996.
24. Qin, G., Zheng, L., Xie, Y. and Wu, C. On the framework hydroxyl groups of H-ZSM-5 zeolites. *Journal of Catalysis*, 95(2):609-612, 1985.
25. Chester, A. W., Chu, Y. F., Dessau, R. M., Kerr, G. T. and Kresge, C. T. Aluminium-independent cation exchange of internal siloxy groups in ZSM-5 and ZSM-11. *Journal of the Chemical Society, Chemical Communications*, 5:289-290, 1985.

26. Hunger, M., Kärger, J., Pfeifer, H., Caro, J., Zibrowius, B., Bülow, M. and Mostowicz, R. Investigation of internal silanol groups as structural defects in ZSM-5-type zeolites. *Journal of the Chemical Society, Faraday Transactions 1: Physical Chemistry in Condensed Phases*, 83(11):3459-3468, 1987.
27. Védrine, J. C., Auroux, A., Bolis, V., Dejaifve, P., Naccache, C., Wierzchowski, P., Derouane, E. G., Nagy, J. B., Gilson, J. P., van Hooff, J. H. and van den Berg, J. P. Infrared, microcalorimetric, and electron spin resonance investigations of the acidic properties of the H-ZSM-5 zeolite. *Journal of Catalysis*, 59(2):248-262, 1979.
28. Jacobs, P. A. and Von Ballmoos, R. Framework hydroxyl groups of H-ZSM-5 zeolites. *The Journal of Physical Chemistry*, 86(15):3050-3052, 1982.
29. Kazansky, V. B., Kustov, L. M. and Borovkov, V. Y. Near infrared diffuse reflectance study of high silica containing zeolites. *Zeolites*, 3(1):77-81, 1983.
30. Datka, J. and Tużnik, E. Infrared spectroscopic studies of acid properties of NaHZSM-5 zeolites. *Journal of Catalysis*, 102(1):43-51, 1986.
31. Kraushaar, B., De Haan, J. W. and Van Hooff, J. H. C. Comment on the letter to the editors written by RM Dessau, KD Schmitt, GT Kerr, GL Woolery, and LB Alemany, entitled “On the presence of internal silanol groups in ZSM-5 and the annealing of these sites by steaming”. *Journal of Catalysis*, 109(2):470-471, 1988.
32. Kraushaar, B., Van De Ven, L. J. M., De Haan, J. W. and Van Hooff, J. H. C. Clusters of terminal groups in ZSM-5: A study performed by silylation and ^{29}Si CP MAS NMR. In *Studies in Surface Science and Catalysis*, volume 37, pages 167-174, Elsevier, 1988.
33. Dessau, R. M., Schmitt, K. D., Kerr, G. T., Woolery, G. L. and Alemany, L. B. On the proposed clustering of silanol groups in ZSM-5. *Journal of Catalysis*, 109(2):472-473, 1988.
34. Kühl G. H. Modification of Zeolites. In: Weitkamp J., Puppe L. *Catalysis and Zeolites*. Pages 81-197, Springer, Berlin, Heidelberg, 1999.
35. Van Bekkum H, Flanigen E. M., Jacobs P and Jensen J. C. *Introduction to Zeolite Science and Practice*. 2nd edition, New York: Elsevier, 2001.

36. Shukla D. B and Pandya V. P. Estimation of crystalline phase in ZSM-5 zeolites by infrared spectroscopy. *Journal of Chemical Technology and Biotechnology*, 44(2):147-154, 1989.
37. Tallon, J. L. and Buckley, R. G. Thermal decomposition of the zeolite catalyst ZSM-5. *Journal of Physical Chemistry*, 91(6):1469-1475, 1987.
38. Moliner, M., Díaz-Cabañas, M. J., Fornés, V., Martínez, C. and Corma, A. Synthesis methodology, stability, acidity, and catalytic behavior of the member ring pores ITQ33 zeolite. *Journal of Catalysis*, 254:101-109, 2008.
39. Bordiga, S., Regli, L., Cocina, D., Lamberti, C., Bjorgen, M. and Lillerud, K. P. Assessing the acidity of high silica chabazite H-SSZ-13 by FTIR using CO as molecular probe: Comparison with H-SAPO-34. *The Journal of Physical Chemistry*, 109(7):2779-2784, 2005.
40. Selli, E. and Forni, L. Comparison between the surface acidity of solid catalysis determined by TPD and FTIR analysis of preadsorbed pyridine. *Microporous and Mesoporous Materials*, 31:129-140, 1993.
41. Lietz, G., Schnabel, K. H., Peuker, C., Gross, T., Storek, W. and Volter, J. Modifications of H-ZSM-5 catalysts by NaOH treatment. *Journal of Catalysis*, 148(2):562-568, 1994.
42. Chang, C. D., Chu, C. T., Miale, J. N., Bridger, R. F. and Calvert, R. B. Aluminum insertion into high silica zeolite frameworks. 1. Reaction with aluminum halides. *Journal of the American Chemical Society*, 106(26):8143-8146, 1984.
43. Dessau, R. M. and Kerr, G. T. Aluminum incorporation into high silica zeolites. *Zeolites*, 4(4):315-318, 1984.
44. Yamagishi, K., Namba, S. and Yashima, T. Preparation and acidic properties of aluminated ZSM-5 zeolites. *Journal of Catalysis*, 121(1):47-55, 1990.
45. Omegna, A., Haouas, M., Kogelbauer, A. and Prins, R. Realumination of dealuminated HZSM-5 zeolites by acid treatment: A reexamination. *Microporous and Mesoporous Materials*, 46(2-3):177-184, 2001.
46. Sano, T., Uno, Y., Wang, Z. B., Ahn, C. H. and Soga, K. Realumination of dealuminated HZSM-5 zeolites by acid treatment and their catalytic properties. *Microporous and Mesoporous Materials*, 31(1-2):89-95, 1999.

47. Fan, Y., Bao, X., Lin, X., Shi, G. and Liu, H. Acidity adjustment of HZSM-5 zeolites by dealumination and realumination with steaming and citric acid treatments. *The Journal of Physical Chemistry B*, 110(31):15411-15416, 2006.
48. Iler, R. K. *The Chemistry of Silica: Solubility, Polymerization, Colloid and Surface Properties and Biochemistry of Silica*, Willey, New York, 1979.
49. Meng, F., Wang, Y., Wang, S. and Wang, S. Hydration of cyclohexene over zeolite ZSM-5: Improved catalyst performance by alkali treatment. *Reaction Kinetics, Mechanisms and Catalysis*, 119(2):671-683, 2016.
50. Kang, J., Cheng, K., Zhang, L., Zhang, Q., Ding, J., Hua, W., Lou, Y., Zhai, Q. and Wang, Y. Mesoporous zeolite-supported ruthenium nanoparticles as highly selective Fischer-Tropsch catalysts for the production of C5-C11 isoparaffins. *Angewandte Chemie International Edition*, 50(22):5200-5203, 2011.
51. Sartipi, S., Parashar, K., Valero-Romero, M. J., Santos, V. P., van der Linden, B., Makkee, M., Kapteijn, F. and Gascon, J. Hierarchical H-ZSM-5-supported cobalt for the direct synthesis of gasoline-range hydrocarbons from syngas: Advantages, limitations, and mechanistic insight. *Journal of Catalysis*, 305:179-190, 2013.
52. Falamaki, C., Edrissi, M. and Sohrabi, M. Studies on the crystallization kinetics of zeolite ZSM-5 with 1, 6-hexanediol as a structure-directing agent. *Zeolites*, 19(1):2-5, 1997.
53. Munnik, P., de Jongh, P. E. and de Jong, K. P. Recent developments in the synthesis of supported catalysts. *Chemical Reviews*, 115(14):6687-6718, 2015.
54. White, R. J., Luque, R., Budarin, V. L., Clark, J. H. and Macquarrie, D. J. Supported metal nanoparticles on porous materials. Methods and applications. *Chemical Society Reviews*, 38(2):481-494, 2009.
55. Zhu, Q. L. and Xu, Q. Immobilization of ultrafine metal nanoparticles to high-surface-area materials and their catalytic applications. *Chem*, 1(2):220-245, 2016.
56. Gates, B. C. Supported metal clusters: Synthesis, structure, and catalysis. *Chemical Reviews*, 95(3):511-522, 1995.
57. Guzman, J. and Gates, B. C. Supported molecular catalysts: Metal complexes and clusters on oxides and zeolites. *Dalton Transactions*, 17:3303-3318, 2003.

58. Cruz-Cabeza, A. J., Esquivel, D., Jiménez-Sanchidrián, C. and Romero-Salguero, F. J. Metal-exchanged β zeolites as catalysts for the conversion of acetone to hydrocarbons. *Materials*, 5(1):121-134, 2012.
59. Oliveira, J. S. D., Mazutti, M. A., Urquieta-González, E. A., Foletto, E. L. and Jahn, S. L. Preparation of mesoporous Fe_2O_3-supported ZSM-5 zeolites by carbon-templating and their evaluation as photo-Fenton catalysts to degrade organic pollutant. *Materials Research*, 19(6):1399-1406, 2016.
60. Kristiani, A., Sudiyarmanto, S., Aulia, F., Hidayati, L. N. and Abimanyu, H. Metal supported on natural zeolite as catalysts for conversion of ethanol to gasoline. In *MATEC Web of Conferences*, volume 101, pages 01001, EDP Sciences, 2017.
61. Kokotailo, G. T., Lawton, S. L., Olson, D. H. and Meier, W. M. Structure of Synthetic Zeolite ZSM-5. *Nature (Lon-don)*, 272:437-438, 1978.
62. Sang, S., Chang, F., Liu, Z., He, C., He, Y. and Xu, L. Difference of ZSM-5 zeolites synthesized with various templates. *Catalysis Today*, 93:729-734, 2004.
63. Liang, J., Liang, Z., Zou, R. and Zhao, Y. Heterogeneous catalysis in zeolites, mesoporous silica, and metal-organic frameworks. *Advanced Materials*, 29(30):1701139, 2017.
64. Jin, M. J., Taher, A., Kang, H. J., Choi, M. and Ryoo, R. Palladium acetate immobilized in a hierarchical MFI zeolite-supported ionic liquid: A highly active and recyclable catalyst for Suzuki reaction in water. *Green Chemistry*, 11(3):309-313, 2009.
65. Fu, W., Liu, T., Fang, Z., Ma, Y., Zheng, X., Wang, W., Ni, X., Hu, M. and Tang, T. High activity and stability in the cross-coupling of aryl halides with disulfides over Cu-doped hierarchically porous zeolite ZSM-5. *Chemical Communications*, 51(27):5890-5893, 2015.
66. Fu, W., Feng, Y., Fang, Z., Chen, Q., Tang, T., Yu, Q. and Tang, T. Zeolite Y nanosheet assembled palladium catalysts with high catalytic activity and selectivity in the vinylation of thiophenes. *Chemical Communications*, 52(15):3115-3118, 2016.
67. Wang, L., Zhang, J., Yi, X., Zheng, A., Deng, F., Chen, C., Ji, Y., Liu, F., Meng, X. and Xiao, F. S. Mesoporous ZSM-5 zeolite-supported Ru nanoparticles as

highly efficient catalysts for upgrading phenolic biomolecules. *ACS Catalysis*, 5(5):2727-2734, 2015.

68. Chen, S., Shao, Z., Fang, Z., Chen, Q., Tang, T., Fu, W., Zhang, L. and Tang, T. Design and synthesis of the basic Cu-doped zeolite X catalyst with high activity in oxidative coupling reactions. *Journal of Catalysis*, 338:38-46, 2016.
69. Zheng, X., Fu, W., Xiong, J., Xi, J., Ni, X. and Tang, T. Zeolite Beta nanoparticles assembled Cu catalysts with superior catalytic performances in the synthesis of thioesters by cross-coupling of aldehydes and disulfides. *Catalysis Today*, 264:152-157, 2016.
70. Dong, H., Zhang, L., Fang, Z., Fu, W., Tang, T., Feng, Y. and Tang, T. Acidic hierarchical zeolite ZSM-5 supported Ru catalyst with high activity and selectivity in the seleno-functionalization of alkenes. *RSC Advances*, 7(36):22008-22016, 2017.
71. Ntais, S., Moschovi, A. M., Paloukis, F., Neophytides, S., Burganos, V. N., Dracopoulos, V. and Nikolakis, V. Preparation and ion transport properties of NaY zeolite-ionic liquid composites. *Journal of Power Sources*, 196(4):2202-2210, 2011.
72. Li, Z. M., Zhou, Y., Tao, D. J., Huang, W., Chen, X. S. and Yang, Z. MOR zeolite supported Brønsted acidic ionic liquid: An efficient and recyclable heterogeneous catalyst for ketalization. *RSC Advances*, 4(24):12160-12167, 2014.
73. Busatta, C. A., Mignoni, M. L., de Souza, R. F. and Bernardo-Gusmão, K. Nickel complexes immobilized in modified ionic liquids anchored in structured materials for ethylene oligomerization. *Applied Sciences*, 8(5):717, 2018.
74. Arya, K., Rawat, D. S. and Sasai, H. Zeolite supported Brønsted-acid ionic liquids: An eco approach for synthesis of spiro [indole-pyrido [3, 2-e] thiazine] in water under ultrasonication. *Green Chemistry*, 14(7):1956-1963, 2012.
75. Arya, K. and Prabhakar, B. Ionic liquid confined zeolite system: An approach towards water mediated room temperature synthesis of spiro [pyrazolo [3, 4-e] benzothiazepines]. *Green Chemistry*, 15(10):2885-2894, 2013.
76. Murthy, Z. V. P. and Modi, A. D. Effect of ionic liquid in Sn-ZSM-5 zeolite membrane in the separation of butyl acetate-water mixtures by pervaporation.

Synthesis and Reactivity in Inorganic, Metal-Organic, and Nano-Metal Chemistry, 43(6):657-661, 2013.

77. Shindo, R., Kishida, M., Sawa, H., Kidesaki, T., Sato, S., Kanehashi, S. and Nagai, K. Characterization and gas permeation properties of polyimide/ZSM-5 zeolite composite membranes containing ionic liquid. *Journal of Membrane Science*, 454:330-338, 2014.
78. Losch, P., Pascual, A. M., Boltz, M., Ivanova, S., Louis, B., Montilla, F. and Odriozola, J. A. Ionic liquid immobilization on carbon nanofibers and zeolites: Catalyst design for the liquid-phase toluene chlorination. *Comptes Rendus Chimie*, 18(3):324-329, 2015.
79. Chincholi, M., Sagwekar, P., Nagaria, C., Kulkarni, S. and Dhokpande, S. Removal of dye by adsorption on various adsorbents: A review. *International Journal of Engineering, Science and Technology*, 3:835-840, 2014.
80. Yagub, M. T., Sen, T. K., Afroze, S. and Ang, H. M. Dye and its removal from aqueous solution by adsorption: A review. *Advances in Colloid and Interface Science*, 209:172-184, 2014.
81. Ajmal, A., Majeed, I., Malik, R. N., Idriss, H. and Nadeem, M. A. Principles and mechanisms of photocatalytic dye degradation on TiO_2 based photocatalysts: A comparative overview. *RSC Advances*, 4(70):37003-37026, 2014.
82. Shore, J. Advances in direct dyes. *Indian Journal of Fiber and Textile Research*, 21:1-29, 1996.
83. Forgacs, E., Cserhati, T. and Oros, G. Removal of synthetic dyes from wastewaters: A review. *Environment International*, 30(7) 953-971, 2004.
84. Galindo, C., Jacques, P. and Kalt, A. Photooxidation of the phenylazonaphthol AO20 on TiO_2: Kinetic and mechanistic investigations. *Chemosphere*, 45(6-7):997-1005, 2001.
85. Kudo, T., Nakamura, Y. and Ruike, A. Development of rectangular column structured titanium oxide photocatalysts anchored on silica sheets by a wet process. *Research on Chemical Intermediates*, 29(6):631-639, 2003.
86. Bahnemann, D. Photocatalytic water treatment: solar energy applications. *Solar Energy*, 77(5):445-459, 2004.

87. Aleboyeh, A., Kasiri, M. B. and Aleboyeh, H. Influence of dyeing auxiliaries on AB74 dye degradation by UV/H_2O_2 process. *Journal of Environmental Management*, 113:426-431, 2012.
88. Huang, H., Leung, D. Y., Kwong, P. C., Xiong, J. and Zhang, L. Enhanced photocatalytic degradation of methylene blue under vacuum ultraviolet irradiation. *Catalysis Today*, 201:189-194, 2013.
89. Surolia, P. K., Lazar, M. A., Tayade, R. J. and Jasra, R. V. Photocatalytic degradation of 3, 3′-Dimethylbiphenyl-4, 4′-diamine (o-Tolidine) over nanocrystalline TiO_2 synthesized by sol-gel, solution combustion, and hydrothermal methods. *Industrial & Engineering Chemistry Research*, 47(16):5847-5855, 2008.
90. Lazar, M. A., Tayade, R. J., Bajaj, H. C. and Jasra, R. V. Correlation of surface properties and photocatalytic activity of nanocrystalline TiO_2 on the synthesis route. In *Nano Hybrids*, volume 1, pages 57-80, Trans Tech Publications, 2012.
91. Chen, H. W., Ku, Y. and Wu, C. Y. Effect of LED optical characteristics on temporal behavior of o-cresol decomposition by UV/TiO_2 process. *Journal of Chemical Technology & Biotechnology: International Research in Process, Environmental & Clean Technology*, 82(7):626-635, 2007.
92. Daniel, D. and Gutz, I. G. Microfluidic cell with a TiO_2-modified gold electrode irradiated by an UV-LED for in situ photocatalytic decomposition of organic matter and its potentiality for voltammetric analysis of metal ions. *Electrochemistry Communications*, 9(3):522-528, 2007.
93. Ohtani, B. Chapter 5. Principle of photocatalysis and design of active photocatalysts. In *New and Future Developments in Catalysis*, pages 121-144, Elsevier Inc., 2013.
94. Guillard, C., Disdier, J., Herrmann, J. M., Lehaut, C., Chopin, T., Malato, S. and Blanco, J. Comparison of various titania samples of industrial origin in the solar photocatalytic detoxification of water containing 4-chlorophenol. *Catalysis Today*, 54(2-3):217-228, 1999.
95. Zeltner, W. A. and Tompkin, D. T. Ashrae Transactions, volume 3, part 2, pages 532, American Society of Heating and Air-Conditioning Engineers Inc., 2005.
96. Fujishima, A. and Honda, K. Electrochemical photolysis of water at a semiconductor electrode. *Nature (London)*, 238:37-38, 1972.

97. Ayodhya, D. and Veerabhadram, G. A review on recent advances in photodegradation of dyes using doped and heterojunction based semiconductor metal sulfide nanostructures for environmental protection. *Materials Today Energy*, 9:83-113, 2018.
98. Fabiyi, M. E. and Skelton, R. L. Photocatalytic mineralisation of methylene blue using buoyant TiO_2-coated polystyrene beads. *Journal of Photochemistry and Photobiology A: Chemistry*, 132(1-2):121-128, 2000.
99. Kim, D. S. and Park, Y. S. Photocatalytic decolorization of rhodamine B by immobilized TiO_2 onto silicone sealant. *Chemical Engineering Journal*, 116(2):133-137, 2006.
100. Shan, A. Y., Ghazi, T. I. M. and Rashid, S. A. Immobilisation of titanium dioxide onto supporting materials in heterogeneous photocatalysis: A review. *Applied Catalysis A: General*, 389(1-2):1-8, 2010.
101. Linsebigler, A. L., Lu, G. and Yates Jr, J. T. Photocatalysis on TiO_2 surfaces: principles, mechanisms, and selected results. *Chemical Reviews*, 95(3):735-758, 1995.
102. Herrmann, J. M., Matos, J., Disdier, J., Guillard, C., Laine, J., Malato, S. and Blanco, J. Solar photocatalytic degradation of 4-chlorophenol using the synergistic effect between titania and activated carbon in aqueous suspension. *Catalysis Today*, 54(2-3):255-265, 1999.
103. Hu, S., Wang, A., Li, X., Wang, Y. and Löwe, H. Hydrothermal synthesis of ionic liquid [Bmim]OH-modified TiO_2 nanoparticles with enhanced photocatalytic activity under visible light. *Chemistry-An Asian Journal*, 5(5):1171-1177, 2010.
104. Dong, T., Xu, Y. Q., Chen, F. W., Chi, Y. N. and Hu, C. W. 1-methyl-3-octylimidazolium polyoxomolybdate ionic liquid with low melting point and high stability: Preparation and photocatalytic activity. *Chemical Research in Chinese Universites*, 27(2):177-180, 2011.
105. Dong, T., Chen, F. W., Cao, M. H. and Hu, C. W. Low melting point and high stability polyoxomolybdate-based ionic liquids as photocatalysts. *Chemical Research in Chinese Universites*, 27(1):11-14, 2011.

106. Wang, Y., Deng, K. and Zhang, L. Visible light photocatalysis of BiOI and its photocatalytic activity enhancement by in situ ionic liquid modification. *The Journal of Physical Chemistry C*, 115(29):14300-14308, 2011.
107. Qi, L., Yu, J. and Jaroniec, M. Enhanced and suppressed effects of ionic liquid on the photocatalytic activity of TiO_2. *Adsorption*, 19(2-4):557-561, 2013.
108. Sajjad, S., Leghari, S. A. K. and Zhang, J. Copper impregnated ionic liquid assisted mesoporous titania: Visible light photocatalyst. *RSC Advances*, 3(31):12678-12687, 2013.
109. Ma, S., Meng, J., Li, J., Zhang, Y. and Ni, L. Synthesis of catalytic polypropylene membranes enabling visible-light-driven photocatalytic degradation of dyes in water. *Journal of Membrane Science*, 453:221-229, 2014.
110. Huo, Y., Hou, R., Chen, X., Yin, H., Gao, Y. and Li, H. BiOBr visible-light photocatalytic films in a rotating disk reactor for the degradation of organics. *Journal of Materials Chemistry A*, 3(28):14801-14808, 2015.
111. Ji, X., Zhang, Q., Qu, X., Wang, Q., Song, X. M., Liang, F. and Yang, Z. Poly (ionic liquid) Janus nanosheets towards dye degradation. *RSC Advances*, 5(28):21877-21880, 2015.
112. Wang, Y. and Guo, J. S. Catalyzed oxidative degradation of methyl orange over Au catalyst prepared by ionic liquid-polymer modified silica. In *IOP Conference Series: Materials Science and Engineering*, volume 87(1), pages 012019, IOP Publishing, 2015.
113. Narayanan, S., Vijaya, J. J., Sivasanker, S., Kennedy, L. J., Kathirgamanathan, P. and Raj, R. A. Synthesis of hierarchical ZSM-5 hexagonal cubes and their catalytic activity in the solvent-free selective oxidation of toluene. *Journal of Porous Materials*, 22(4):907-918, 2015.
114. Shirazi, L., Jamshidi, E. and Ghasemi, M. R. The effect of Si/Al ratio of ZSM-5 zeolite on its morphology, acidity and crystal size. *Crystal Research and Technology: Journal of Experimental and Industrial Crystallography*, 43(12):1300-1306, 2008.
115. Jansen, J. C., Van der Gaag, F. J. and Van Bekkum, H. Identification of ZSM-type and other 5-ring containing zeolites by IR spectroscopy. *Zeolites*, 4(4):369-372, 1984.

116. Fan, W., Li, R., Ma, J., Fan, B. and Cao, J. Synthesis, characterization and catalytic properties of MFI-type zeolites prepared in the system Na_2O SiO_2 Al_2O_3 H_2N (CH_2) $6NH_2$ NH_4F. *Microporous Materials*, 4(4):301-307, 1995.
117. Jacobs, P. A., Beyer, H. K. and Valyon, J. Properties of the end members in the Pentasil-family of zeolites: Characterization as adsorbents. *Zeolites*, 1(3):161-168, 1981.
118. Coudurier, G., Naccache, C. and Vedrine, J. C. Uses of IR spectroscopy in identifying ZSM zeolite structure. *Journal of the Chemical Society, Chemical Communications*, 24:1413-1415, 1982.
119. Saikia, S., Gogoi, P., Dutta, A. K., Sarma, P. and Borah, R. Design of multifaceted acidic 1, 3-disulfoimidazolium chlorometallate ionic systems as heterogeneous catalysts for the preparation of β-amino carbonyl compounds. *Journal of molecular catalysis A: Chemical*, 416:63-72, 2016.
120. Yamagishi, K., Namba, S. and Yashima, T. Defect sites in highly siliceous HZSM-5 zeolites: A study performed by alumination and IR spectroscopy. *The Journal of Physical Chemistry*, 95(2):872-877, 1991.
121. Isernia, L. F. FTIR study of the relation, between extra-framework aluminum species and the adsorbed molecular water, and its effect on the acidity in ZSM-5 steamed zeolite. *Materials Research*, 16(4):792-802, 2013.
122. Groen, J. C., Moulijn, J. A. and Pérez-Ramírez, J. Desilication: On the controlled generation of mesoporosity in MFI zeolites. *Journal of Materials Chemistry*, 16(22):2121-2131, 2006.
123. Zhang, Y., Zhou, Y., Huang, L., Xue, M. and Zhang, S. Sn-modified ZSM-5 as support for platinum catalyst in propane dehydrogenation. *Industrial & Engineering Chemistry Research*, 50(13):7896-7902, 2011.
124. Khatamian, M. and Irani, M. Preparation and characterization of nanosized ZSM-5 zeolite using kaolin and investigation of kaolin content, crystallization time and temperature changes on the size and crystallinity of products. *Journal of the Iranian Chemical Society,* 6(1):187-194, 2009.
125. Fan, F., Sun, K., Feng, Z., Xia, H., Han, B., Lian, Y., Ying, P. and Li, C. From molecular fragments to crystals: A UV Raman spectroscopic study on the mechanism of Fe-ZSM-5 synthesis. *Chemistry-A European Journal*, 15(13):3268-3276, 2009.

126. Zanjanchi, M. A. and Ebrahimian, A. Studies on the solid-state ion exchange of nickel ions into zeolites using DRS technique. *Journal of Molecular Structure*, 693(1-3):211-216, 2004.
127. Thommes, M., Kaneko, K., Neimark, A. V., Olivier, J. P., Rodriguez-Reinoso, F., Rouquerol, J. and Sing, K. S. Physisorption of gases, with special reference to the evaluation of surface area and pore size distribution (IUPAC Technical Report). *Pure and Applied Chemistry*, 87(9-10):1051-1069, 2015.
128. Vafi, L. and Karimzadeh, R. A novel method for enhancing the stability of ZSM-5 zeolites used for catalytic cracking of LPG: Catalyst modification by dealumination and subsequent silicon loading. *Chinese Journal of Catalysis*, 37(4):628-635, 2016.
129. Kore, R., Srivastava, R. and Satpati, B. ZSM-5 zeolite nanosheets with improved catalytic activity synthesized using a new class of structure-directing agents. *Chemistry-A European Journal*, 20(36):11511-11521, 2014.
130. Voogd, P., Scholten, J. J. F. and Van Bekkum, H. Use of the t-plot-De Boer method in pore volume determinations of ZSM-5 type zeolites. *Colloids and Surfaces*, 55:163-171, 1991.
131. Dedecek, J., Sobalik, Z., Tvaruazkova, Z., Kaucky, D. and Wichterlova, B. Coordination of Cu ions in high-silica zeolite matrixes. Cu^+ photoluminescence, IR of NO adsorbed on Cu^{2+}, and Cu^{2+} ESR study. *The Journal of Physical Chemistry*, 99(44):16327-16337, 1995.
132. Yang, X., Tiam, T. S., Yu, X., Demir, H. V. and Sun, X. W. Europium (II)-doped microporous zeolite derivatives with enhanced photoluminescence by isolating active luminescence centers. *ACS Applied Materials & Interfaces*, 3(11):4431-4436, 2011.
133. Pradhan, A. C., Sahoo, M. K., Bellamkonda, S., Parida, K. M. and Rao, G. R. Enhanced photodegradation of dyes and mixed dyes by heterogeneous mesoporous Co-Fe/Al_2O_3–MCM-41 nanocomposites: Nanoparticles formation, semiconductor behavior and mesoporosity. *RSC Advances*, 6(96):94263-94277, 2016.
134. Deka, P., Deka, R. C. and Bharali, P. Porous CuO nanostructure as a reusable catalyst for oxidative degradation of organic water pollutants. *New Journal of Chemistry*, 40(1):348-357, 2016.

135. Li, T., Sun, T., Aftab, T. B. and Li, D. Photocatalytic degradation of methylene blue in aqueous solution using ceramsite coated with micro-Cu_2O under visible-light irradiation. *Korean Journal of Chemical Engineering*, 34(4):1199-1207, 2017.
136. Chanderia, K., Kalal, S., Sharma, J., Ameta, N. and Punjabi, P. B. Heterogeneous photo-Fenton like degradation of rhodamine B using copper loaded bentonite and H_2O_2. *Indian Journal of Chemistry*, 52A:1416-1420, 2013.
137. Tang, M. L., Oh, J. H., Reichardt, A. D. and Bao, Z. Chlorination: A general route toward electron transport in organic semiconductors. *Journal of the American Chemical Society*, 131(10):3733-3740, 2009.
138. Tang, M. L. and Bao, Z. Halogenated materials as organic semiconductors. *Chemistry of Materials*, 23(3):446-455, 2010.
139. Wang, F., Chen, Y., Zhu, R. and Sun, J. Novel synthesis of magnetic, porous C/$ZnFe_2O_4$ photocatalyst with enhanced activity under visible light based on the Fenton-like reaction. *Dalton Transactions*, 46(34):11306-11317, 2017.
140. Chithambararaj, A., Sanjini, N. S., Bose, A. C. and Velmathi, S. Flower-like hierarchical h-MoO_3: New findings of efficient visible light driven nano photocatalyst for methylene blue degradation. *Catalysis Science & Technology*, 3(5):1405-1414, 2013.